Accessible remote sensing of water

Burggraaff, O.

1 | General introduction

Water is all around us. We use it to drink, wash, play, fish, sail, and much more. Natural waters, like streams, rivers, lakes, seas, and oceans, are full of life and interesting chemistry. Because of its importance, we need to study water intensively, measuring the various compounds and life forms that inhabit it. This way, we can better understand the world around us, our impact on it, and its impact on us.

Light is a powerful tool for studying water. Humans and other animals can intuitively infer some properties of water from its colour and clarity. Using many different wavelengths and other properties of light provides a wide spectrum of information. In remote sensing, we aim to determine the chemical and biological makeup of water by measuring how it reflects light. These measurements can be done on a global scale over long periods of time, without needing to physically sample the water. Automated remote sensing instruments can also provide data on more local scales quickly and with consistent quality.

Because water is so important to everyone, participation in water research should be widely accessible. Citizen science involves non-professionals in taking measurements, interpreting results, and thinking of new research. Citizens provide many data and local knowledge that, in collaboration with professional researchers, can lead to new possibilities and shared insights. At the same time, the citizen scientists learn more about their environment by conducting their own research and they are socially and politically empowered as stakeholders.

This introduction provides a general overview of the field. Section 1.1 introduces the various constituents of global surface waters. In Section 1.2, we look at light and how it is measured. Section 1.3 combines the two by discussing remote sensing of water. Section 1.4 is about citizen science in water research. Each section discusses the current state of research, challenges, and future opportunities. Finally, Section 1.5 provides an overview of the main chapters in this thesis, which focus on various aspects of accessibility and uncertainty in remote sensing.

Accessibility here means the degree to which people can create, use, and interpret data. In Chapter 2, we investigate and improve the ability of people with a disability, namely colour blindness, to participate in water research by performing colour measurements. In Chapters 3 and 4, we develop and validate a method for using consumer cameras, especially on smartphones, to perform professional-grade measurements at a low cost. In Chapter 6, we present iSPEX 2, a new smartphone add-on for remote sensing measurements. The ability to use consumer cameras opens up remote sensing to people without expensive professional instruments, for example people in low-income settings and in citizen science.

Uncertainty here refers to the spread in measured values caused by random effects and to errors caused by known or unknown systematic effects. To use data to their fullest potential, it is crucial to determine, understand, and minimise the associated uncertainty. In Chapter 2, we investigate the uncertainty in water colour measurements by citizen scientists due to colour blindness. In Chapters 3 and 4, we determine and minimise the uncertainty in measurements from consumer cameras by characterising and calibrating their response. Lastly, in Chapter 5, we determine the impact of a common mathematical error in comparing data from different instruments.

1.1 Water

Water is one of the most important resources on Earth and it plays a central part in all aspects of our lives [1, 2]. Clean drinking water is crucial to human health and wellbeing, and many cultures and religions attribute cleansing properties to water itself. Recreation, such as water sports, provides further social value. Economic value lies in the use of water in agriculture, energy generation, fishery, industry, and infrastructure. Of course, humans are not alone on Earth, and water is equally important to all other life forms. In fact, the detection of liquid water is seen as an essential step in the search for extraterrestrial life [3]. Given the many important roles water plays in our lives, it is imperative that we study its biological and chemical constituents and their interactions well.

Social and political discussions on water often focus on the concept of *water quality* [4–8], but this term is misleading. The meaning of water quality is inherently subjective and varies by subject and by stakeholder. For example, most people naturally judge the quality of water for recreation by its aesthetics and think of clear, blue waters as having a high water quality [9]. However, such blue waters are often lacking in nutrients and many algae would consider them low quality [10], if algae could speak. Discussing natural waters in terms of their *quality* thus introduces a human-centric bias and narrows our field of view. It is better to consider nature from a broader perspective that includes humans as part of a greater whole [11]. Even in the United Nations Sustainable Development Goals (SDGs), biodiversity and ecosystem health are primarily considered means towards human-centric ends such as economic growth, rather than goals unto themselves [12].

Scientifically, we are interested in the many processes, substances, and organisms in surface waters, together referred to as *biogeochemistry*. Studying the properties of a water body provides an understanding of its ecosystem and physics. This knowledge is valuable in itself, and further scientific and social value is derived by, for example, improving our understanding of the role of the oceans in climate change adaptation [2] and detecting events that affect human and animal health, such as harmful algal blooms [13].

Environmental regulations typically consist of chemical measures, such as maximum concentrations for pollutants, and ecological indicators, such as targets for population size, species richness, biodiversity indices, and population viability. Monitoring of these variables is performed by all levels of governmental and private parties through extensive sampling and laboratory analysis. Within the water management community, there is a desire to shift the focus of monitoring programmes from individual concentrations to a full understanding of water bodies through systems analysis [7]. Biodiversity is seen as an important proxy for ecosystem health and as a means to improve the resilience of ecosystems against change [4,5]. High biodiversity is also a goal in itself, as it provides an inherent existence value [1].

This thesis focuses on the characterisation of surface waters through optical observations from above the surface. What follows in Sections 1.1.1–1.1.3 is a brief overview of surface water biogeochemistry, separated into inorganic constituents, organic constituents, and pollution. Lastly, Section 1.1.4 discusses challenges relating to the observation of water properties through traditional measurement methods.

1.1.1 Inorganic constituents

Oceans and inland waters contain a wide variety of dissolved and particulate inorganic material. The distinction between dissolved and particulate is typically drawn at a particle size

of 0.2 µm or 0.7 µm. While each substance contributes to the optical and biogeochemical properties of a water body in its on way, most fit into one of several major categories, which are discussed below [14].

Important quantities relating to dissolved inorganic material include salinity, pH, and concentrations of oxygen and trace elements [2, 5]. Salinity is the concentration of dissolved ions and is commonly measured in situ by lowering a conductivity-temperature-depth (CTD) probe into the water to obtain a vertical profile [15]. Seawater has a typical salinity of ~35 g kg^{-1}, consisting primarily of sodium chloride (Na^+ and Cl^-) [16], and a slightly alkaline pH of ~8.1 [17]. Most inland waters are fresh, meaning the salinity is near-zero, with a typical pH of 6.0–8.5 [18], influenced by surrounding land cover, evaporation rates, and other environmental factors [15, 19]. Increasing absorption of atmospheric CO_2 is decreasing ocean pH, a process called *acidification* [20], causing decreased growth rates of organisms with calcite shells like corals and coccolithophorid algae [20, 21]. Some dissolved trace chemicals play a role in biological processes, such as iron ions in photosynthesis and cell structure [21, 22], while others like mercury are toxic [23]. Trace chemical concentrations are traditionally determined from field samples, requiring extensive sample preparation and expensive laboratory equipment and causing a delay between sampling and results [23]. Lastly, dissolved oxygen (O_2) concentrations range from near-zero to $\gtrsim$360 µmol kg^{-1} [24]. Animals and other aerobic organisms require oxygen to function, and insufficient dissolved oxygen levels lead to mass death. Large algal blooms resulting from a sudden influx of nutrients, such as iron from a volcanic eruption, can decrease oxygen levels below habitable conditions and kill millions of animals within days [2, 13]. Dissolved oxygen is measured using in-situ optical and electrochemical sensors or through laboratory analysis of samples [25, 26].

Particulate inorganic material consists of suspended sediments and minerals [14, 27], ranging in size from several µm to >10 mm [28, 29]. The concentration of particulate inorganic material is described by several quantities with different, partially overlapping definitions, some of which also include particulate organic material (Section 1.1.2). Commonly reported quantities include mineral suspended sediment (MSS), suspended particulate matter (SPM), total suspended matter (TSM), total suspended solids (TSS), detritus, and turbidity [14, 27, 30–34]. The quantity of choice depends on the specifics of the measurement site, application, and available methods and materials. Suspended inorganic matter is supplied by erosion of the shoreline and bottom, in the water body itself or in supplying rivers and tributaries, and by deposition of atmospheric aerosols [28, 33, 35]. Particulate matter that has settled can be resuspended by water currents, particularly in shallow waters with high wind speeds and in tidal areas [27, 29, 33]. The dynamic nature of the processes supplying suspended matter can lead to highly variable concentrations. For example, SPM concentrations ranging from <1–4000 g m^{-3} have been observed in the Wadden Sea [29]. Because many sediments scatter light strongly (Section 1.3.1), variations in SPM induce variations in the amount of photosynthetically available radiation and thus affect phytoplankton and vegetation populations [35].

Suspended matter concentrations are determined in the laboratory by filtering and optionally drying water samples [35, 36]. The variability between replicate measurements is typically 1–5%, with outliers of ≥10% [37]. The particle size distribution can be inferred from the forward scattering of light (Section 1.3.1), for example using a Sequoia LISST instrument [14, 28]. Portable turbidimeters are relatively low-cost and easy to use, and provide in-situ measurements of turbidity with an uncertainty of 1–3% [37]. TSM or SPM can be derived from turbidity with a mean bias as low as 2% and root-mean-square (RMS) error

of 25% using a well-tuned algorithm, but due to spatial and temporal variability in particle properties, these errors can be ≥50% in some sites [38, 39]. In general, variability between replicate in-situ measurements is caused by both measurement uncertainty and inherent variability [40].

1.1.2 Organic constituents

The ocean and other surface waters are host to a wide variety of organisms and organic materials, ranging in size from dissolved proteins to blue whales [14]. While each contributes to the ecosystem in its own way, here we will focus on phytoplankton and coloured dissolved organic matter (CDOM). Both are important biogeochemical components of virtually all surface waters and are commonly studied through visible-light remote sensing [2, 41].

Phytoplankton is a broad category of free-floating microscopic organisms that perform primary production of organic compounds through photosynthesis. The most prominent taxonomical groups are green algae, coccolithophorids, diatoms, dinoflagellates, and cyanobacteria [14]. Species may alternatively be classified by their role in the ecosystem or *functional type* to better understand nutrient cycles. Important functional types include nitrogen fixers, which bind dissolved nitrogen into nutrients; calcifiers, which produce calcium carbonate shells; and silicifiers, which produce structures of silica. Carbonate and silica structures aggregate and sink, exporting nutrients from the surface to deeper layers. Diversity is necessary to provide and distribute all nutrients required in the ecosystem and thus to maintain population levels, biodiversity, and resilience to change [42]. Phytoplankton are responsible for half of the global primary production of organic matter and oxygen, contribute significantly to the global carbon cycle, and form the basis of the marine food web [14,43,44]. This high ecological importance makes phytoplankton biomass and taxonomic as well as functional diversity essential biodiversity and climate variables [43, 45].

Phytoplankton has fast growth and reproduction cycles, so it responds rapidly to changes in environmental conditions and nutrient availability, on a time scale of hours or days. These changes can cause algal blooms, during which one species rapidly increases in biomass and dominates the local ecosystem [13, 46]. For example, number concentrations of *Phaeocystis* algae of up to 100 000 cm^{-3} were observed during the 1994 spring and summer blooms in the Marsdiep, Netherlands, while almost none were found between blooms [46]. Changes in phytoplankton biomass and diversity serve as a proxy for overall changes in the ecosystem and rapid detection of algal blooms is required to mitigate harmful effects such as toxins released into the water [13]. Many inland waters, particularly in the Netherlands, are currently undergoing a strong increase in phytoplankton contents (*eutrophication*) and harmful algal bloom frequency due to pollution with nutrients such as nitrogen and phosphorus. These trends are causing major social and economic problems by decreasing oxygen concentrations and introducing toxins into the water, in turn disrupting the food chain, killing aquatic animals, and preventing the use of surface waters for drinking, irrigation, and recreation [1, 4, 5, 47]. For example, cyanobacterial blooms induced by emission of phosphorus are dangerous to swimmers, since exposure to cyanobacteria can cause skin irritation, gastrointestinal disease, and even death [48].

Chlorophyll-a (*chl-a*) and other chemical pigments are used by phytoplankton for photosynthesis. Different types of phytoplankton use different pigments, based on niches in the absorption spectrum of water [49]. Pigment concentrations are used to quantify phytoplankton biomass and differentiate between species. Chl-a is the most important pigment [42] and

ranges in concentration from 0.01–100 mg m^{-3} in the ocean and most inland waters [50, 51]. Chl-a is so dominant that its concentration alone is enough to describe the optical properties of most of the open ocean (*Case I* waters) since all other constituents largely covary with it [52]. Aside from chl-a, important pigments include other types of chlorophyll, carotenoids, and the cyanobacteria-specific pigments phycocyanin and phycoerythrin [49, 53]. Photosynthesis is performed using visible light with wavelengths of 400–700 nm, also termed photosynthetically active radiation (PAR) [49].

There are several common methods for in-situ detection and characterisation of phytoplankton. High-performance liquid chromatography (HPLC) is used to accurately measure pigment concentrations, and thus infer the biomass of different phytoplankton types, and is the standard for calibration and validation of other methods [42, 50]. A major drawback of HPLC is its high cost and labour intensity. Intercomparisons of HPLC measurements of the same samples by different teams have yielded reproduction uncertainties of 5–40% in chl-a concentration, which were ascribed to differences in HPLC protocol [54]. Many pigments fluoresce (Section 1.3.1) and the intensity of fluorescence at different wavelengths is a proxy for pigment concentrations [52, 53]. Fluorescence measurements can be done at a low cost using a light emitting diode (LED) or laser light source [55, 56] and typically agree well with HPLC [50]. For example, a comparison between 402 simultaneous HPLC and fluorometric chl-a concentrations from five oceanic sites yielded a median absolute difference of 11% [57]. However, the conversion from intensity to pigment concentration is complicated by the distribution of pigments inside the algal cells and sensitivity to fluctuating light levels [42]. Determination of pigment concentration from other inherent optical properties is discussed in Section 1.3.3. Imaging techniques such as microscopy and flow cytometry detect and characterise individual cells and other suspended matter. These methods are labour-, equipment-, and compute-intensive, but this is rapidly improving and machine learning classification algorithms with >80% accuracy (precision and recall) have been demonstrated [43]. Lastly, genomics can accurately distinguish between hundreds of species based on sampled (meta-)genomes [58].

Dissolved organic matter (DOM) is created by biological processes in a water body or its sources, or is introduced into the water body from the bottom or from surrounding land [59]. DOM consists of thousands of different organic compounds. Some of these compounds strongly absorb light and thus change the appearance of the water (Section 1.3.1) – together, these compounds are called *chromophoric* or *coloured dissolved organic matter* (CDOM) [25]. The terms *yellow substance* and *gelbstoff* are also used [60]. Absorption by CDOM gives many peat lakes in the Netherlands, such as the Kagerplassen near Leiden, their characteristic dark brown colour by removing blue–green light from the reflectance spectrum, leaving only yellow–red light (Section 1.3.3). CDOM is a tracer for DOM, but the exact relation depends on the concentrations of specific chemicals and varies by location and over time [14, 25]. Often, one is specifically interested in the amount of carbon dissolved in the water in various compounds, for example when studying the carbon cycle or climate change. In that case, the closely related quantity *dissolved organic carbon* (DOC) is used [25]. The DOC concentration is 0.2–2.0 g m^{-3} in the ocean [61] and ranges from near-zero to >20 g m^{-3} in lakes and rivers [25, 62, 63]. DOM, CDOM, and DOC are typically studied with optical techniques based on fluorescence or absorption [60, 64], discussed further in Section 1.3.1, or with catalytic oxidation systems [25, 65].

1.1.3 Pollution

In addition to their natural constituents, most surface waters contain some degree of pollution by humans. This pollution comes in many forms, from dissolved molecules to metre-scale debris, and from many sources. Faecal matter from humans and other animals is a major threat to drinking water safety in many parts of the world [1, 66], including historically in the Netherlands [67]. Excreta are also a major vector for pollution with pharmaceuticals, which can have severe impacts on aquatic animals [5, 68]. Agricultural runoff can induce eutrophication and algal blooms by adding nutrients to the water (Section 1.1.2), or alternatively decimate ecosystems by unintentional emission of pesticide residue through various routes such as runoff, leaching, drift, and aerosol deposition [69]. These effects cascade through the food web and affect all members of an ecosystem [69]. The forms of pollution described above are detected through chemical monitoring and ecological surveillance data [5, 18, 69]. Within the European Union, the establishment of programmes for water monitoring and surveillance is required by the Water Framework Directive [8].

Solid debris comes in many forms, including wood, food waste, cloth and fabric, metal, glass, and plastics [70]. Plastic pollution is particularly commonly researched and discussed currently because of its close relation to human activities, its broad and persistent distribution across global waters [71–74], and its far-reaching, albeit still debated, effects on individual organisms and ecosystems [5, 73]. Plastic particles range in size from the nano- and micrometre-scale (*nanoplastics* and *microplastics*) to large objects like shopping bags (*macroplastics*). Smaller particles are released through weathering and breakdown of large objects, but also aggregate into larger clusters through the creation of biofilms and integration into organic matter [73]. Microplastic surface densities in the ocean are typically 1 g km^{-2}–1 kg km^{-2}, but can reach up to 100 kg km^{-2} in the Pacific garbage patch [75]. Plastics and other debris are detected through in-situ soil and water samples and photographs from ships and other platforms, but protocols are not sufficiently standardised and different methods often yield different results [76, 77]. An integrated observation system with remote sensors (Section 1.3) is required to monitor pollution with debris on all spatial and temporal scales with high accuracy [75].

1.1.4 Challenges and opportunities

Characterisation of surface water constituents through in-situ sampling faces three main challenges, namely cost of equipment and labour; availability of data on different spatial and temporal scales; and reproducibility between researchers, sites, and methodologies.

As discussed in Sections 1.1.1–1.1.3, many constituents require trained personnel and expensive laboratory equipment to measure. For example, an HPLC measurement of chl-a in a lake requires researchers to sail out on a ship, take and properly store a water sample, bring the sample to a laboratory for filtering and extraction, run it through an HPLC instrument costing several thousand euros, and analyse the results using specialised software. Even with economies of scale, such as measuring multiple parameters per sample and taking many samples per cruise, the cost per HPLC chl-a measurement is on the order of hundreds of euros. Other methods like fluorometric analysis have a lower cost per sample, but come with greater uncertainties. Cost and labour requirements limit the scope of constituent monitoring at large spatial scales and high frequencies, and disproportionately limit the accessibility of data in low-income settings, which often bear the brunt of environmental problems caused by pollution and climate change [1, 11].

In general, in-situ measurements are difficult to scale up spatially and temporally. Global coverage is necessary to understand global processes like climate change, but the funds and personnel required to physically sample every water body regularly are not available. Research into local processes, for instance in individual lakes and other inland waters, is similarly constrained by the lack of scaleability of in-situ measurements. Moreover, while early detection of rapid events such as harmful algal blooms saves money and lives, laboratory analysis cannot provide the required high-frequency measurements and rapid responses [2].

Lastly, standardisation in sampling and analysis protocols between researchers, both locally and internationally, is limited [78]. Chl-a concentrations measured simultaneously by different teams differ by as much as 5–40% (Section 1.1.2). Due to differences in measurement protocol and reporting of results, it is nearly impossible to quantitatively compare microplastic loads across the world [77]. This lack of reproducibility between data from different periods or areas creates spurious trends and is difficult to detect or correct post hoc, as samples cannot be stored and re-used indefinitely. The issue is further exacerbated by scant reporting of uncertainty.

Three important opportunities towards meeting these challenges are automation, remote sensing, and citizen science. Automation enables large-scale, high-frequency measurements with reproducible results. Remote sensing reduces the cost of sample processing, can be performed on all spatial and temporal scales, and is highly reproducible. Citizen science can significantly decrease the cost per measurement and increase both the scale and quality of measurements by including more people in the scientific process and incorporating local knowledge. Each of the three opportunities is discussed in more detail below.

In recent years, autonomous platforms have increasingly been used to provide high-quality, reproducible data at a relatively fine spatial and temporal resolution. For example, the Argo array consists of nearly 4 000 robotic floats, which in the last 20 years have provided over 2 million CTD profiles covering most of the ocean [79]. Many Argo floats are now also equipped with bio-optical sensors to measure chl-a and other biogeochemical parameters [80]. Similarly, underwater gliders can autonomously perform horizontal and vertical transects for up to six months at a time [81]. Gliders and floats have been used together to measure variations in density, chl-a concentration, and primary production with sub-kilometre spatial resolution [82]. These autonomous platforms provide high-quality data, but they are limited by high purchase and use costs and are less suitable for shallow and inland waters. In-line flow-through systems installed on research vessels and ships of opportunity use water pumped into the vessel to automatically perform bio-optical measurements with high frequency and reliability. By combining professional instruments such as the aforementioned LISST, Sea-Bird AC-s transmissometer, and Sea-Bird ECO series scattering meters with an automated pumping system and data logger, the data volume can be massively increased and the cost per measurement decreased [83, 84]. While automation is not discussed in detail in this thesis, some of our findings can be applied or extrapolated to automated sensors, as discussed in the individual chapters.

Remote sensing is a measuring technique that does not require physically sampling a water body, instead relying on reflected light to carry information. Satellite remote sensing of water started in earnest in the 1970s and has evolved continually since then [85], with the forthcoming Plankton, Aerosol, Cloud, ocean Ecosystem (PACE) mission [86] as the most prominent new development (Sections 1.2.2, 1.2.3, and 1.3.3). Operational remote sensing platforms include satellites, aeroplanes and uncrewed aerial vehicles (UAVs or drones), ships, and terrestrial instruments [31, 87]. Remote sensing provides data with wide spatial

coverage over long periods, and with sufficient resolution, precision, and accuracy for many practical applications [2, 88]. For example, satellite data are used to rapidly detect and warn against potentially harmful algal blooms anywhere in the global ocean and many inland waters, with a speed and coverage that cannot be achieved with traditional sampling-based techniques [13]. Terrestrial and shipborne remote sensing provides high-frequency data with fast response times and high reproducibility, since data are recorded electronically and can thus be processed automatically and near-instantly [89, 90]. The uncertainty in measurements of reflected light is typically $\lesssim$5% for a single instrument [88], as is the reproducibility between different instruments [91, 92]. The physics of measuring light are discussed in Section 1.2 and the implementation and application of remote sensing in Section 1.3.

Citizen science, the involvement of non-professionals in the scientific process, provides further opportunities to reduce cost and improve scalability by increasing the accessibility of water research. Citizens are important stakeholders in water management and thus offer valuable *bottom-up* perspectives and insights to research aims and methods [93]. Through *crowd-sourcing*, citizens massively increase data collection capabilities [94], on large spatial scales and over long periods as well as on the local level and with fast response times. There are various degrees of citizen involvement, ranging from data collection for a *top-down* research project to co-creation of an entirely new project [95]. Citizen science is discussed in more detail in Section 1.4.

1.2 Detection of light

To understand remote sensing, it is useful to first understand the physics of light itself. Fundamentally, light consists of electromagnetic (EM) waves, quantised into discrete packets of energy called *photons*. EM waves are generated by various processes involving the acceleration of electrically charged particles and propagate outward at $c = 299\,792\,458$ m s^{-1}. For EM waves in free space, the electric and magnetic field vectors oscillate orthogonally to the direction of propagation and to each other. Defining properties of individual photons include wavelength, spin angular momentum or polarisation, and orbital angular momentum. Remote sensing instruments gather many photons within one exposure, so this thesis focuses on the bulk properties of light fields consisting of many photons. For a comprehensive description of remote sensing from basic physical principles, the reader is referred to [14, 96].

The fundamental observable quantity of remote sensing is spectral radiance L, the radiant power emitted or received by a surface, as defined in Equation (1.1) and illustrated in Figure 1.1. $\vec{L}$ is the radiance at a position $\vec{x}$ and time t, from a direction $\hat{\xi}$, at a nominal wavelength λ; ΔQ is the energy emitted or received by a surface ΔA over a time Δt, within a wavelength range $\Delta\lambda$ and a solid angle $\Delta\Omega$ [14]. Radiance is written as a vector $\vec{L}$ when polarisation is considered or as a scalar L when polarisation is neglected. Radiance has units of W m^{-2} nm^{-1} sr^{-1}.

$$\vec{L}(\vec{x}, t, \lambda, \hat{\xi}) = \frac{\Delta Q}{\Delta A\, \Delta t\, \Delta\lambda\, \Delta\Omega} \tag{1.1}$$

Another important quantity is planar irradiance E, which is the total radiance integrated over a hemisphere, as shown in Equation (1.2). For example, the downwelling irradiance E_d represents the total radiant power received by a surface, such as a patch of sea, from all upwards directions [97]. Irradiance has units of W m^{-2} nm^{-1}.

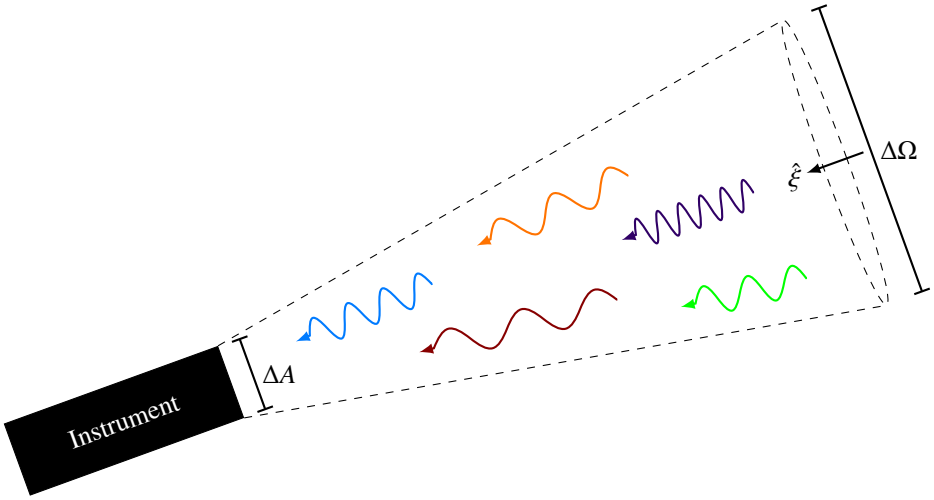

Figure 1.1: Schematic representation of a radiometric instrument detecting incoming light, represented by several photons with different wavelengths. ΔA is the collecting area of the instrument, $\hat{\xi}$ the observing direction, and $\Delta\Omega$ the solid angle subtended by the field of view, indicated by dashed lines. Note that photons travel in straight lines, as indicated by the arrowheads; the waves indicate the direction of the oscillating electric field.

$$E(\vec{x}, t, \lambda) = \frac{\Delta Q}{\Delta A \, \Delta t \, \Delta \lambda} \tag{1.2}$$

The following subsections provide a brief description of the measurement of radiance in general (1.2.1), as a function of wavelength (1.2.2), and considering polarisation (1.2.3). The use of radiometry in remote sensing is discussed in Section 1.3.

1.2.1 Radiometry

Currently, most scientific instruments and consumer cameras are based on charge-coupled device (CCD) or complementary metal-oxide-semiconductor (CMOS) sensors [14, 98, 99]. CCD and CMOS sensors use the photo-electric effect to detect incoming photons that strike a layer of semiconductor and, if they have enough energy, free one or more electrons [100], which are called *photo-electrons*. The number of photo-electrons generated per photon is the quantum efficiency η, which is highly wavelength-dependent [101]. CCD and CMOS sensors typically contain millions of µm-sized pixels for high-resolution imaging and spectrometry. Other sensor types of historical relevance include bolometers [99] and photographic plates and film [102, 103]. This thesis mostly deals with CMOS sensors, which are by far the most common in consumer cameras [98].

The collected photo-electrons are converted to a voltage, which is then amplified and digitised [101]. CMOS sensors include amplification and digitisation electronics on individual pixels, enabling pixel-level control. For example, the amplifier gain, the conversion factor from photo-electrons to volts, can be varied between pixels to compensate for differences in sensitivity (Section 3.4.6). Many CMOS amplifiers have built-in compensation for non-linearity and other sources of uncertainty [104], although additional corrections are sometimes necessary [105]. An analogue-to-digital converter (ADC) is used to digitise the ampli-

fied voltage into analogue-digital units (ADU). The ADC bit depth determines the number of possible digital values, which was as low as 128 (7-bit) for early satellite instruments [96], but is now more typically in the range of 4 096–65 536 possible values (12–16-bit).

The raw data in ADU are converted to radiant energy ΔQ through a radiometric calibration [106]. First, the optical properties of the instrument, including the sensor and any fore-optics, are characterised (Chapter 3). Next, an absolute radiometric calibration is performed, in which the sensor observes a light source with known characteristics to determine the conversion factor from ADU to physical units [107, 108]. Ideally, the materials used in the calibration and characterisation are traceable to standards such as those maintained by the National Institute of Standards and Technology (NIST, USA) or the National Physical Laboratory (NPL, UK) [106, 108].

Professional field-going and satellite instruments are calibrated and characterised by their manufacturers prior to delivery. Field-going instruments are certified to sub-percent radiometric accuracy at most wavelengths and the reproducibility between different instruments under realistic conditions is normally 1–5% [92, 109, 110], as discussed further in Chapter 4. Satellite instruments require sub-percent accuracy and uncertainty, or equivalently a signal-to-noise ratio (SNR) $\geq$100, in some cases $\geq$1000, to deliver percent-level accuracy and uncertainty on ground-level radiance, reflectance, and derived parameters [45, 111, 112]. Calibration is repeated regularly during sensor lifetimes to account for changes in performance. The sensitivity of field-going spectroradiometers typically drifts by $\leq$5% per year, often more strongly in their first years and $\leq$1% later on, although individual instruments may drift by as much as 40% year-to-year [108]. Changes in sensitivity tend to be wavelength-dependent. For satellite instruments, regular vicarious calibration using well-known targets such as the MOBY buoy site and the Moon is used to maintain the desired accuracy and uncertainty of $\sim$5% in reflectance [113]. For consumer cameras, the calibration process is left to the user (Chapter 3).

Common sources of uncertainty include stray light; non-zero sensitivity to wavelengths outside the desired spectral range; sensitivity to polarisation for unpolarised radiance measurements; changes in response due to fluctuations in temperature, humidity, and other environmental factors; degradation of transmission due to fouling by dust, oils, biofilms, and sea spray; shot noise due to the quantum nature of photons; and uncertainties in the calibration materials themselves [108, 110, 114–117]. The relative contribution of each component is highly variable between different instruments and varies by wavelength and over time.

Observations are done over a limited exposure time Δt to obtain the radiant power $\frac{\Delta Q}{\Delta t}$. The exposure time is ideally as long as possible before the sensor saturates. Individual exposures are realised by physically blocking the sensor from incoming light with a mechanical shutter or by electronically powering the sensor on and off [99]. An advantage of mechanical shutters over electronic shutters is the ability to take fully dark exposures for calibration purposes; a disadvantage is the reliance on moving parts, which eventually malfunction or break. In either case, it is important to characterise the accuracy and reproducibility of the shutter to ensure accurate radiance measurements [118, 119].

A well-collimated radiometer detects light from a viewing direction $\hat{\xi} = (\theta, \phi)$. The simplest well-collimated instrument is the Gershun tube, a long tube with multiple baffles to select only light from within a narrow field of view around the desired $\hat{\xi}$ [14]. The instrument can be moved or rotated to observe in multiple directions sequentially, which is called *pushbroom* or *whiskbroom* sensing. Many instruments use lenses to focus incoming light onto a sensor array, in which each pixel corresponds to a viewing direction. Field radiome-

ters are typically aligned on a mount which is fixed in, or swivels to, the desired viewing direction [120]. Some systems must be aligned by eye [121, 122], others are fully automated [123, 124]. The required pointing accuracy and stability depend on the application, but are typically 0.5°–5° for instruments mounted on stationary observing platforms [124, 125].

The radiometer fore-optics also determine its collecting area ΔA and field of view (FOV) $\Delta\Omega$. The collecting area is ideally as large as possible to collect more light and thus improve the SNR, but is usually limited by physical restrictions. ΔA is on the order of mm^2–cm^2 for field radiometers [126] and consumer cameras (Section 3.4.1), and up to hundreds of cm^2 for satellite instruments [14]. The desired value of $\Delta\Omega$ depends on the application, particularly on the degree of isotropy in the target. Most spot radiometers for above-water radiometry have 1°–7° FOVs [105, 108, 126], equivalent to a solid angle $\Delta\Omega$ of 10^{-4}–10^{-2} sr. For imaging systems, it is important to geometrically calibrate the FOV for individual pixels, which may vary due to distortions induced by the fore-optics [99, 107].

1.2.2 Spectroradiometry

Spectroradiometry is the process of measuring the distribution (*spectrum*) of photons or radiance across different wavelengths λ. Absorption and scattering alter the spectrum of light as it travels through a medium (Section 1.3.1). The full spectrum of light includes gamma rays, x-rays, ultraviolet (UV), visible light, infrared (IR), microwave, and radio waves. The same physics apply to light at all wavelengths, although with differences in sensor design and performance, and all are used for remote sensing. This thesis focuses on visible light, with λ between 390–700 nm. This spectral range covers the sensitivity of the human eye and most consumer cameras (Chapters 2 and 3), and contains all photosynthetically active radiation (PAR) [49].

The wavelength of a photon is inversely proportional to its frequency and energy, which is $\sim 10^{-19}$ J for visible-light photons. For illustration, the typical visible-range clear-sky solar irradiance of ~400 W m^{-2} corresponds to $\sim 10^{21}$ photons s^{-1} m^{-2} [14]. In a medium, the speed and wavelength of light are decreased by a factor n, the *refractive index*. Typical values of n are $1.000\,293 \approx 1$ in air and 1.33–1.35 in water, depending on its constituents; n itself also varies by wavelength [14, 127].

CCD and CMOS sensors detect photons with different wavelengths, but cannot distinguish between wavelengths. Therefore, performing spectroradiometry requires additional optical elements. The most common techniques are moveable or tuneable filters, patterned filters, and dispersion with a grating or prism (Figure 1.2). Each method is briefly described below; for a more general overview, the reader is referred to [128, 129].

Before proceeding, it is important to define some terms. *Spectral filters* are optical elements that preferentially transmit certain wavelengths. A spectral filter or *band* B has a *spectral response function* (SRF), $S_B(\lambda)$, describing its transmittance at each wavelength λ. The SRF of an instrument is the product of its filter SRFs, the transmission efficiency of other optical elements, and the sensor quantum efficiency (Section 1.2.1). SRFs are often defined in terms of their central wavelength λ_c and bandwidth or *spectral resolution* $\Delta\lambda$. Typically, λ_c is taken to be the wavelength with the highest transmittance or the SRF-weighted average wavelength, and $\Delta\lambda$ is the SRF full width at half maximum (FWHM). A *multispectral* instrument measures in discrete bands, while a *hyperspectral* instrument covers a continuous wavelength range (Figure 1.3). Following the Shannon-Nyquist theorem, the *spectral sampling*, which is the difference between successive wavelengths in hyperspectral data, needs to

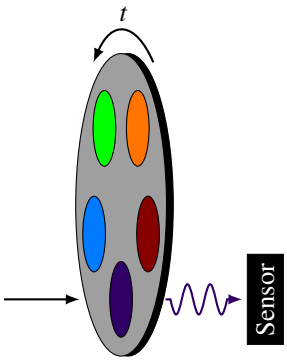

(a) Spectral filters in a rotating filter wheel. Incoming broad-spectrum light (black arrow) passes through one filter at a time, transmitting only specific wavelengths (purple arrow) to the sensor.

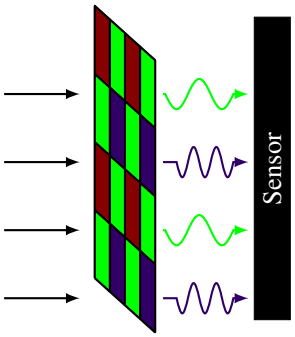

(b) Spectral filters in a Bayer pattern. Incoming broad-spectrum light (black arrows) passes through one filter for each pixel, transmitting the corresponding wavelengths (coloured arrows) to the sensor. For clarity, only four light rays are shown.

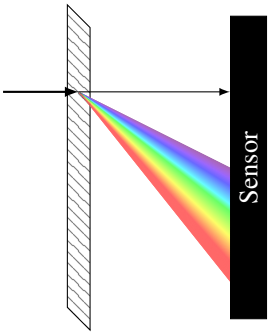

(c) Dispersive spectrometer setup. Incoming broad-spectrum light (black arrow) is dispersed by a grating or prism and transmitted to the sensor (black arrow, spectrum). For clarity, only a single incoming light ray is shown here.

Figure 1.2: Schematic representation of three techniques for spectroradiometry.

be half the spectral resolution or finer. The terms spectral resolution and spectral sampling are often confused in the literature, but they are fundamentally different quantities. A commonly used criterion for the *hyperspectral* label is $\Delta\lambda \lesssim 10$ nm in >20 continuous bands, but the distinction with multispectral is ultimately subjective [14, 87]. Methods for comparing and combining the two are discussed in Chapter 5.

The simplest method for spectroradiometry is a rotating wheel with individual filters corresponding to spectral bands of interest, mounted in front of a sensor (Figure 1.2a). A major advantage of this method is the use of the same sensor for each measurement, removing the need for many calibration steps when performing relative measurements such as reflectance band ratios (Section 1.3.2). A major disadvantage is the delay between measurements in successive bands, which makes this method unsuitable for targets that move or

(a) Multispectral data cover a few discrete spectral bands.

(b) Hyperspectral data cover a continuous wavelength range.

Figure 1.3: Multispectral and hyperspectral data.

vary over time scales comparable to the rotation period of the filter wheel, and sensitive to vibrations in the instrument [130]. Rotating filter wheels are used in satellite instruments including GOCI [131] and POLDER 1–3 [132] and in many ground-based spectroradiometers [117,119,133,134]. A variation on the technique, commonly used in satellite instruments, is using fixed filters on different pixels in one sensor, which observe the target sequentially (pushbroom) due to the orbital movement of the satellite [135]. Finally, some instruments instead employ a single filter with a tuneable SRF, such as a Fabry-Pérot etalon [136] or variable liquid crystal retarder between polarising filters [137].

Virtually all consumer cameras employ a patterned Bayer filter [138] with red-green-blue (RGB) bands (Section 3.2). These have wide SRFs (Section 3.4.8) and are arranged in a checkerboard pattern on top of the sensor, with two green filters for every red or blue one (Figure 1.2b). Each pixel observes in a single band and a *demosaicking* algorithm is used to interpolate the results and form a combined multispectral image [139, 140]. The main advantage of patterned filters is the ability to take snapshot multispectral images, with no delay between filters or between parts of the image. Disadvantages include the need to calibrate the response of each individual pixel before band ratios can be calculated and uncertainties introduced by the demosaicking algorithm, especially for targets with sharp features, which can create spurious edge effects when comparing the different channels. New variations on the method mitigate these disadvantages through additional colour filters and different filter arrangements [139, 141].

The third major technique is spectral dispersion through a prism or grating (Figure 1.2c). Many variations exist, including transmission and reflection gratings and integrated lens-grating or grating-prism systems [128, 142]. Because the entire spectrum is dispersed across the sensor, data can be obtained hyperspectrally rather than being limited to hand-picked filters as in the previous two methods. The dispersion takes up one dimension of the sensor array, requiring incoming light to first pass through a point aperture, one-dimensional slit, or integral-field unit to reduce the spatial dimensionality. Imaging is performed through whisk- or pushbroom sensing. The properties of the dispersive element and the width of the entrance pupil or slit determine the spectral resolution, while the size and number of pixels in the sensor determine the spectral sampling (Section 6.5.3). Spectral dispersion is highly suitable for hyperspectral spot radiometers and satellite instruments [86, 116, 126]. A dispersive element can also be mounted onto an existing camera [94, 143]; the design and performance of such an add-on, iSPEX 2, are discussed in Chapter 6.

The optimal design choices for a spectroradiometer depend on the application and technical constraints. On paper, measuring at more wavelengths λ and with a narrower bandwidth $\Delta\lambda$ provides more information about the target and is thus desirable. However, the wavelength range is limited by technical factors such as the quantum efficiency and size of the sensor. Furthermore, for a given aperture and exposure time, narrower bandwidths lead to a lower SNR, decreasing the effective information content of a signal [144]. Finally, the increase in information content with a finer sampling or wider range of wavelengths may be smaller than expected due to correlations in the spectrum at different wavelengths [145, 146]. Thus, instruments are best designed with their desired application in mind. For example, AERONET-OC was built to validate radiometric data from pre-existing multispectral satellite instruments, meaning only a small number of pre-determined spectral bands were needed and a relatively simple rotating filter wheel design could be used [117]. When studying a substance with distinct, well-known spectral features, only a handful of spectral bands covering those features and any applicable calibrations are necessary.

The most commonly used instruments for above-water spectroradiometry are the TriOS RAMSES and Sea-Bird HyperOCR [92, 114]. They cover wavelengths of 320–950 nm and 350–800 nm, respectively, both with a bandwidth of ∼10 nm and spectral sampling of 3.3 nm [147, 148]. Also commonly used are the Malvern Panalytical ASD FieldSpec, which covers 350–2500 nm with a 3 nm bandwidth [149], and the Water Insight WISP-3, which covers 380–800 nm with a 5 nm bandwidth [126]. Each of these instruments covers the entire visible range, which includes the spectral features of important constituents like chl-a, CDOM, and suspended particles (Section 1.3.1). The additional near-infrared (NIR) coverage of the RAMSES and ASD enables cross-calibration between NIR wavelengths, where no signal is expected, and visible wavelengths [90]. The typical accuracy and reproducibility of these instruments is on the percent level (Section 1.2.1). The WISP-3 suffers from normalisation issues when compared to other instruments [126], as discussed in detail in Chapter 4. Other field-going spectroradiometers of note include the DALEC [109], PANTHYR [124], WISPstation [89], and the SeaPRISM instrument used for AERONET-OC [117].

At the core of satellite instrumentation design is the trade-off between extending capabilities and maintaining a sufficient SNR. For example, the Operational Land Imager (OLI) on Landsat 8 and 9 has a fine spatial sampling of 30 m per pixel, but is consequently limited to relatively wide spectral bands, with bandwidths of ≥40 nm for the blue, green, red, and NIR bands [135]. Conversely, the Ocean and Land Colour Instrument (OLCI) on the Sentinel-3 satellites features 21 bands from 400–1020 nm with a narrow 10 nm bandwidth, and a much coarser spatial sampling of 300 m per pixel, at a sensitivity of $\sim 10^{-3}$ W m^{-2} sr^{-1} nm^{-1} [150]. The MultiSpectral Imager (MSI) on Sentinel-2 combines both approaches, having 9 bands in the visible-NIR range with bandwidths of 15–115 nm and spatial resolutions of 10–60 m [151]. Other satellite instruments of note include the Sea-Viewing Wide Field-of-View Sensor (SeaWiFS), Moderate Resolution Imaging Spectroradiometer (MODIS), Visible Infrared Imaging Radiometer Suite (VIIRS), and Geostationary Ocean Color Imager (GOCI) [131, 152]. Successive generations of satellite instruments have been built with continuity in mind, for example by maintaining certain spectral bands [152]. Finally, 2024 will see the launch of the Plankton, Aerosol, Cloud, ocean Ecosystem (PACE) satellite, which primarily consists of the Ocean Color Instrument (OCI). OCI is a hyperspectral instrument that provides continuous coverage of wavelengths of 340–890 nm with 5 nm bandwidth [86]. PACE will also carry the SPEXone and HARP-2 spectropolarimeters (Section 1.2.3). For a broader overview of satellite instruments used in remote sensing of water, the reader is referred to [2, 41, 131, 153].

The human eye is essentially a patterned multispectral radiometer and can thus be used as a scientific instrument. The retina contains two types of photosensitive cells, namely rods and cones. Rods are extremely sensitive to light at all visible wavelengths and are highly useful in low-light conditions, but cannot distinguish between wavelengths. The cones contain groups of proteins sensitive to either long (L), medium (M), or short (S) wavelengths (Figure 1.4). The LMS cones are spread around the retina and by comparing their measurements, the brain estimates the spectrum of the incoming radiance. We perceive this as colour [101, 154]. Many animals' eyes function similarly but with different numbers of cones and different SRFs. A number of scientific techniques use the human eye as a sensor to perceive brightness, colour, distance, and other quantities (Section 1.4). A few percent of the human population have some degree of *colour deficiency* or *colour blindness*, meaning their perception of colour is different to that of the average human [155]. Remote sensing of water by citizen scientists with colour blindness is explored in Chapter 2.

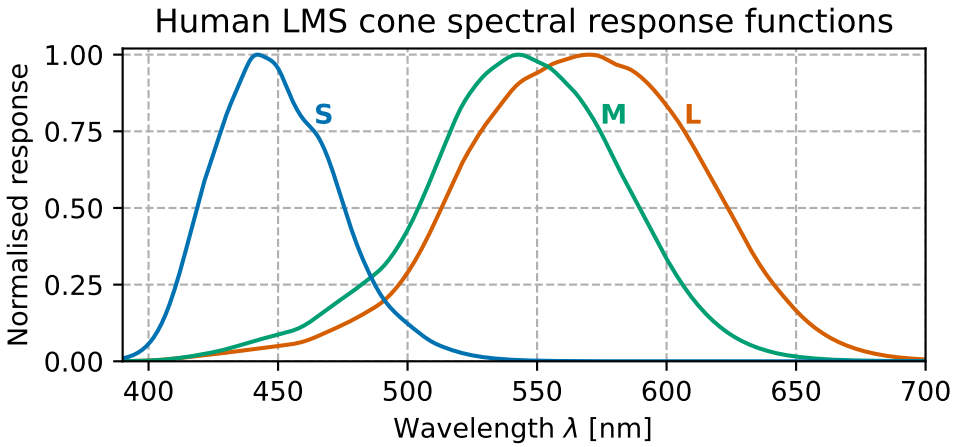

Figure 1.4: Normalised spectral response functions of the long-, medium-, and short-wavelength (LMS) cones in the average human eye. Data obtained from http://www.cvrl.org/.

1.2.3 Spectropolarimetry

Spectropolarimetry is the process of measuring radiance and polarisation at different wavelengths. Polarisation is a wave property of light, relating to the direction of oscillation of the electric[1] field vector $\vec{E}$ as light propagates. For light propagating in the z direction, $\vec{E}$ has components E_x, E_y in the (x, y) plane orthogonal to z.

Light exhibits various polarisation states. These are most easily understood by considering coherent light, for instance from a laser, which behaves like a single wave. As the electric field oscillates, $\vec{E}$ traces a shape in the (x, y) plane, determined by the phase delay δ between the oscillations in E_x and E_y. For example, if E_x and E_y oscillate in phase ($\delta = 0°$), $\vec{E}$ traces a straight line in the (x, y) plane and the light is *linearly polarised*. If E_x and E_y oscillate exactly out of phase ($\delta = 180°$), the light is linearly polarised at the supplementary angle. If E_x and E_y have the same amplitude and oscillate with a delay of $\delta = 90°$, $\vec{E}$ traces a circle in the (x, y) plane and the light is *circularly polarised*. In the general case, $\vec{E}$ traces an ellipse and the light is *elliptically polarised*. The polarisation state of coherent light is described through Jones calculus, combining E_x and E_y into a vector, the Jones vector, and representing optical elements as linear transformations of this vector [116, 156].

Natural light is an incoherent sum of many individual light waves, each with its own polarisation state, resulting in a bulk polarisation state of the light field. When the polarisation states of the constituent EM waves are uniformly randomly distributed, the light is *unpolarised*. If the distribution instead has a preferential direction or handedness, the light is *partially polarised*. Finally, despite being incoherent, the EM waves in *fully polarised* light all have the same polarisation state. For a further physical description of polarisation in natural light, the reader is referred to [157].

This thesis deals with linear polarisation of incoherent light in remote sensing of water (Chapter 6 and Section 7.3). For discussions on remote sensing of the atmosphere with linear polarisation and of vegetation with circular polarisation, the reader is referred to [116, 158].

[1] Because the magnetic field vector is always perpendicular to the electric field vector, it need not be considered separately.

Polarisation of incoherent light is described through Mueller calculus, which generalises Jones calculus but disregards coherent phenomena. Polarised radiance is quantified through the Stokes vector, as in Equation (1.3). $\vec{L}$ is the radiance Stokes vector, I the total radiance, Q the difference in radiance between the horizontal and vertical polarisation states ($I_{\leftrightarrow} - I_{\updownarrow}$), U between the two diagonal polarisation states, and V between right- and left-handed circular polarisation[2]. Any direction can be chosen as the reference *horizontal* $+Q$ direction. For most experiments and models, there is a natural choice, such as the direction of a particular polarising filter, the sky, or the sea surface. The vertical and diagonal directions are defined relative to the horizontal [156]. I is given by $I = I_{\leftrightarrow} + I_{\updownarrow} = I_{\nearrow} + I_{\nwarrow} = I_{\circlearrowleft} + I_{\circlearrowright}$. In cases where it is more intuitive to discuss polarisation in relative terms, the Stokes vector is normalised to the fractional polarisation $q, u, v = \frac{Q}{I}, \frac{U}{I}, \frac{V}{I}$.

$$\vec{L} = \begin{bmatrix} I \\ Q \\ U \\ V \end{bmatrix} = \begin{bmatrix} I_{\leftrightarrow} + I_{\updownarrow} \\ I_{\leftrightarrow} - I_{\updownarrow} \\ I_{\nearrow} - I_{\nwarrow} \\ I_{\circlearrowleft} - I_{\circlearrowright} \end{bmatrix} \tag{1.3}$$

Linearly polarised radiance is often described in terms of the *degree of linear polarisation* (DoLP, P_L) and *angle of linear polarisation* (AoLP, ϕ_L), as defined in Equation (1.4). P_L ranges from 0 (no net polarisation) to 1 (fully polarised), ϕ_L from 0° (horizontal or $+Q$) through 90° (vertical or $-Q$) to 180° (horizontal or $+Q$), or equivalently from 0 to π radians. Because of symmetry (the 180° ambiguity), $\phi_L = 185°$ is equivalent to $\phi_L = 5°$.

$$P_L = \frac{\sqrt{Q^2 + U^2}}{I} \qquad \phi_L = \frac{1}{2} \arctan2\,(U, Q) \tag{1.4}$$

Direct sunlight is unpolarised, for all practical purposes, with $P_L < 10^{-6}$ [159], while diffuse skylight is partially linearly polarised by single scattering of sunlight in the atmosphere [160]. For a clean sky without any aerosols, viewed at 90° from the Sun, $P_L \approx 0.7$ at visible wavelengths. Multiple Rayleigh scattering by air molecules prevents P_L from reaching 1.0, while multiple scattering by aerosols can reduce P_L further, down to 0.5 on a hazy day and as low as 0.2 when smoke is present [161]. Sky polarisation is also decreased by reflections from clouds and the ground. For example, an effective ground albedo of 0.8 decreases P_L by as much as 0.3 compared to an albedo of 0 [162]. Polarisation also occurs due to scattering by particles in water [163, 164], specular reflection off surfaces [165], and interaction with *birefringent* materials such as coccolithophores [21].

In birefringent materials, the refractive index n depends on the polarisation state, being smaller along the *fast axis* and greater along the *slow axis*. This difference induces a phase delay δ as polarised light travels through the material. Optical elements designed to induce a specific δ are called *retarders* or *wave plates*. For example, the optical path through a $\frac{\lambda}{4}$ retarder or quarter-wave plate (QWP) is extended by $\frac{\lambda}{4}$ for light polarised along the slow axis, inducing a phase delay of $\delta_{\mathrm{QWP}} = 90°$ between the fast and slow axes. A QWP with a vertical fast axis converts fully right-handed circularly polarised light ($q = u = 0, v = 1$) to linearly polarised light with $\phi_L = 135°$ ($q = 0, u = -1, v = 0$).

[2] I, Q, U, V are sometimes referred to as S_0, S_1, S_2, S_3, and alternative sign conventions for Equation (1.3) are sometimes used.

The interaction between polarised light and a medium or object is described by the Mueller matrix **M**, as defined in Equation (1.5). The Stokes vector of the outgoing radiance is the product of the incoming Stokes vector with the Mueller matrix, $\vec{L}_{\text{out}} = \mathbf{M}\vec{L}_{\text{in}}$. By determining the elements of **M**, which often vary with wavelength and viewing geometry [166, 167], the properties of a target can be inferred [168].

$$\mathbf{M} = \begin{bmatrix} M_{I\to I} & M_{Q\to I} & M_{U\to I} & M_{V\to I} \\ M_{I\to Q} & M_{Q\to Q} & M_{U\to Q} & M_{V\to Q} \\ M_{I\to U} & M_{Q\to U} & M_{U\to U} & M_{V\to U} \\ M_{I\to V} & M_{Q\to V} & M_{U\to V} & M_{V\to V} \end{bmatrix} \tag{1.5}$$

In the same way that wavelength increases the dimensionality of remote sensing data, and spectroradiometry on a two-dimensional sensor requires additional optics (Figure 1.2), so does measuring polarisation. Measurements techniques for spectropolarimetry fall into three categories, namely temporal, spatial, and spectral modulation [169, 170]. Temporal modulation involves sequential measurements at different angles, similarly to the use of spectral filters (Section 1.2.2). The linear polarisation state can be determined by measuring at 0°, 60°, and 120°; using more angles reduces the uncertainty. Multiple filters are arranged in a filter wheel (Figure 1.2a) or a single filter is rotated or tuned [132, 171]. The time delay between measurements in different polarisation states can create spurious signals when the target moves or changes on a similar time scale. Spatial modulation involves simultaneous measurements of different polarisation directions on different parts of one sensor, through a patterned filter (Figure 1.2b) or by projecting multiple images on the sensor [172, 173]. Alternatively, multiple sensors can be used, either in completely separate, co-aligned instruments or in one instrument using shared fore-optics and a polarising beam splitter [160, 163, 174]. A major challenge for spatial modulation is the appearance of false signals due to misalignment or intercalibration issues between sensors or pixels [160, 172].

Most relevant to this thesis is spectral modulation (sometimes called channelled polarimetry) through the SPEX technique. SPEX encodes the polarisation state into the observed spectrum using a highly chromatic multi-order retarder (MOR) [175]. Because the phase delay or *retardance* δ induced by the MOR varies strongly with λ, the polarisation state of light is modified with a known, wavelength-dependent modulation. When the light is passed through an analysing polarisation filter and dispersed, the resulting spectrum displays a sinusoidal modulation corresponding to the resulting polarisation state. The amplitude of the modulation corresponds to P_L and its phase to ϕ_L (Figure 1.5). By measuring in two channels I_1, I_2 corresponding to orthogonal analysing polarisers, for example through a polarising beamsplitter or a double aperture (Chapter 6), the full linear polarisation state can be retrieved using a demodulation algorithm. The total radiance I is recovered from $I = I_1 + I_2$, while P_L and ϕ_L are recovered by fitting a sinusoidal modulation to the normalised signal $\frac{I_1 - I_2}{I_1 + I_2}$ [116]. Because there are no moving parts and the light is spectrally dispersed, SPEX enables snapshot hyperspectral polarimetry. Existing implementations include groundSPEX [116, 125, 176], iSPEX [94], SPEX Airborne [177], and SPEXone, which will soon fly on the PACE mission [86, 112]. In Chapter 6, we present iSPEX 2 and discuss its design, manufacturing, and data processing. Results from a recent experiment with groundSPEX are discussed in Section 7.3.

Instruments are assessed on their polarimetric sensitivity and accuracy. The *polarimetric sensitivity* of an instrument is the smallest polarisation signal it can detect, and is usually limited by the uncertainty in the individual measurement channels and by spurious signals

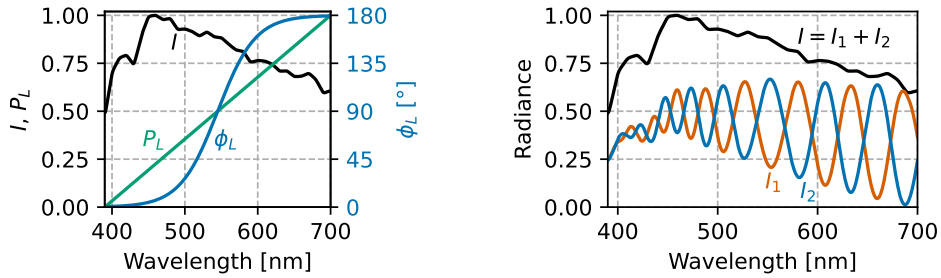

(a) Input spectrum with I (black), P_L (green), and ϕ_L (blue).

(b) Spectrum observed by SPEX instrument, with I_1 in red and I_2 in blue, and the total radiance $I = I_1 + I_2$ in black.

Figure 1.5: Simulated SPEX observations (right) of polarised light (left). A normalised average European daylight spectrum (CIE D65) was used for the total radiance I. The P_L and ϕ_L spectra were constructed to illustrate the technique and are not physical. On the right, the sinusoidal modulation is clearly visible in both SPEX channels, I_1 and I_2, which correspond to orthogonal polarising filters (0° and 90°, respectively) and thus display a 180° modulation phase difference. As P_L increases, so does the modulation amplitude. The shift in ϕ_L from 500–600 nm is reflected by a change in modulation phase in the SPEX data.

due to instrumental or environmental causes. For detectable signals, the *polarimetric accuracy* expresses how well the measured polarisation state describes the true polarisation state of the incoming radiance, accounting for instrumental polarisation and depolarisation as well as cross-talk between the polarisation channels. The accuracy is affected by the physical characteristics of the instrument as well as the data processing and analysis. The observed polarisation state is particularly sensitive to instrumental polarisation caused by systematic errors in the individual measurement channels [116, 169]. Polarimetric accuracy and sensitivity are often conflated in the literature as the *polarimetric uncertainty*.

Compared to unpolarised spectroradiometry, there are relatively few instruments for spectropolarimetry of water. Research has historically been focused on the polarisation of the underwater light field [178]. Many studies have characterised the effects of various constituents on the Mueller matrix of water, for example by measuring the Stokes vector of scattered laser light at varying angles for phytoplankton and suspended particles [164, 179]. Spectropolarimetry above the surface is often conducted by adding polarising filters to spectroradiometers like the HyperOCR [180, 181]. The Mantis instrument, built by Polaris, measures linear polarisation hyperspectrally at 382–1017 nm with an uncertainty of ≤2.5% in radiance, ≤0.5% in P_L, and ≤0.5° in ϕ_L [171]. The mantis is in use by the US Naval Research Laboratory for spectropolarimetry of water [182]. Sony recently released their IMX250MYR and IMX250MZR sensors, featuring four polarisation filters (0°, 45°, 90°, 135°) in a Bayer pattern with an optional additional layer of RGB pixels. Initial results from observing floating debris with one of these sensors are presented in Section 7.3. For a broader review of spectropolarimetric remote sensing of water, the reader is referred to [165].

The most prominent satellite-based spectropolarimeters have been the POLarization and Directionality of the Earth's Reflectances (POLDER) instruments on the ADEOS and PARASOL satellites [132, 165, 180, 183]. The latest, POLDER-3, flew in 2004–2013 and measured

polarised radiance at 490 nm, 670 nm, and 865 nm, in addition to 7 unpolarised bands at 443–1020 nm, at 16 viewing angles between −51° and +51° relative to nadir and with a spatial resolution of ∼6 km per pixel [132]. As discussed previously, POLDER 1–3 measured polarised radiance using a filter wheel rotated to 0°, 60°, and 120° sequentially, with a polarimetric accuracy of 8.5×10^{-4} in P_L [180].

The upcoming PACE mission will feature the SPEXone and HARP-2 spectropolarimeters [86]. SPEXone, designed and built in the Netherlands, uses the SPEX technique to measure radiance and linear polarisation hyperspectrally at 385–770 nm with a 2 nm resolution in radiance and 20–40 nm resolution in P_L. It observes at five viewing angles (0°, ±20°, and ±57° from nadir) and has a spatial sampling of 2.3×2.7 km^2 per pixel. Lastly, the expected uncertainty in SPEXone data is 2% in radiance and 0.0025 in P_L [112,184]. Unlike SPEXone, HARP-2 is multispectral and hyperangular, measuring at 10 viewing angles in three spectral bands (440, 550, and 870 nm) and at 60 viewing angles at 670 nm, spanning 114°. Its ground pixel size is similar to that of SPEXone, at 3 km, and its expected polarimetric accuracy is <0.005 in P_L [86, 185]. SPEXone and HARP-2 are primarily intended for observations of atmospheric aerosol [185], but will also be used in conjunction with OCI for remote sensing of water [186–188]. Other satellite spectropolarimeters of note include the Directional Polarimetric Camera (DPC) on the GaoFen-5 mission [107, 189], and the upcoming PolCube cubesat [190]. For a broader review of satellite spectropolarimetry, though with a focus on aerosols, the reader is referred to [132].

Some animals, including humans, can also sense polarisation. For example, some insects navigate using sky polarisation [191] and mantis shrimp famously see linear and circular polarisation [192]. With training, humans can see linear polarisation as Haidinger's and Boehm's brushes [193, 194].

1.3 Remote sensing of water

Remote sensing is a technique for observing a target without physically sampling it. This thesis is focused on optical remote sensing, using light as the information carrier, of surface waters. Alternative approaches exist, such as acoustic sensing, but are not discussed here. Furthermore, we focus on *passive remote sensing*, using reflected sun- and skylight. The alternative, *active remote sensing*, involves the use of a custom, controllable light source, for example for lidar measurements.

Current platforms for remote sensing of water include in-situ spectroradiometers that are hand-held or mounted on a platform, uncrewed aerial vehicles (UAVs or drones), aeroplanes, and satellites. Each platform has an associated cost, spectral and spatial coverage and resolution, revisit time, and sensitivity. This thesis focuses primarily on the validation and application of smartphone cameras as in-situ spectroradiometers (Chapters 3, 4, and 6), along with the human eye (Chapter 2) and the principles behind comparing different instruments and platforms (Chapter 5).

Remote sensing provides solutions to many of the challenges posed in Section 1.1.4. Autonomous instruments like satellites and in-situ radiometers significantly reduce the expense and labour requirements of continuous measurements. Earth observation of aquatic ecosystems with satellite sensors enables global measurements of water constituents, which in turn enables research on global issues such as climate change. Reducing the dependence on physical sampling and human labour improves the consistency over time and between sensors,

facilitating decade-long time series with a high degree of reproducibility. Lastly, since data are obtained and processed electronically, remote sensing can provide near-instant response times. Since remote sensing does not directly probe the same parameters as in-situ sampling, but instead probes the proxies discussed below, it is not a one-to-one replacement, but rather a complementary method.

In this section, we discuss the physics and practice of remote sensing of water. First, the inherent optical properties of water constituents are discussed (Section 1.3.1), followed by the apparent optical property of reflectance (Section 1.3.2), from which optical parameters and constituents are retrieved (Section 1.3.3). Lastly, Section 1.3.4 discussed the practical aspect of validation.

1.3.1 Inherent optical properties

The interaction between light and water is described by the *inherent optical properties* (IOPs) of the water column [14, 195]. The IOPs are the coefficients of *absorption* a, *scattering* b, and *beam attenuation* c, all in m^{-1}. This c is not to be confused with the speed of light. Absorption converts light into chemical or thermal energy, while scattering shifts energy into different directions of propagation and, in inelastic scattering, wavelengths. Beam attenuation is the sum of the two, as in Equation (1.6), and describes the exponential decay in radiant power as light passes through water, following Lambert's law as in Equation (1.7). Here $L(x, \lambda)$ is the radiance at wavelength λ after travelling a distance x through the water column. For illustration, $c = 0.7\ \mathrm{m}^{-1}$ means the radiance is halved for every metre travelled.

$$a + b = c \tag{1.6}$$

$$L(x, \lambda) = L(0, \lambda)\, e^{-c(\lambda)x} \tag{1.7}$$

Absorption is highly wavelength-dependent and many constituents of natural waters (Section 1.1) have characteristic absorption spectra (Figure 1.6). Adding the constituent absorption spectra together gives the total absorption spectrum in the water column. The major absorbing constituents are phytoplankton, CDOM, and non-algal particles (NAP). NAP refers to particles that do not contain extractable pigments [14]. Water itself is highly absorbing at longer wavelengths, hence its blue appearance [49, 196].

Phytoplankton primarily absorbs through pigments with characteristic spectral signatures. The average phytoplankton absorption spectrum is dominated by a narrow chl-a peak around 665 nm and a broad peak around 442 nm (Figure 1.6), primarily caused by chl-a and broadened by other chlorophylls such as chl-b and chl-c as well as by carotenoids such as β-carotene, fucoxanthin, and zeaxanthin [14, 199]. The cyanobacterial pigment complexes phycocyanin and phycoerythrin can cause additional absorption peaks or shoulders around 495 nm, 550–570 nm, and 630 nm [49]. Phytoplankton absorption spectra are broadened and flattened by formation of pigment-protein complexes and packing of pigment inside cellular structures, both of which change the vibration energies of molecular bonds. The precise shape and magnitude of the spectrum depend on the species present and on cell characteristics that vary over the diurnal cycle [14, 88]. For a detailed review of pigments found in various classes of phytoplankton, the reader is referred to [200].

The absorption spectra of CDOM and NAP also depend on their composition, but can be approximated by an exponential function in λ, as shown in Equation (1.8). Here $a(\lambda_0)$ is the

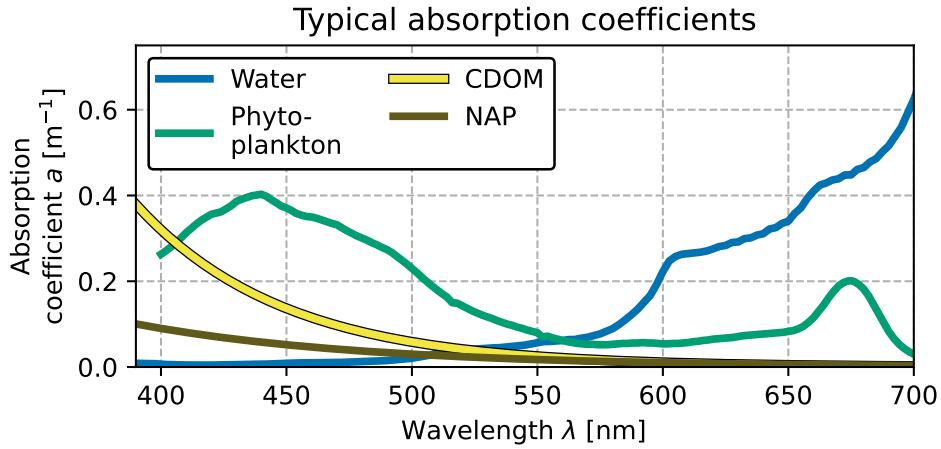

Figure 1.6: Typical spectral absorption coefficients $a(\lambda)$ of water, phytoplankton (at 10 mg m^{-3} chl-a), CDOM ($a(400\text{ nm}) = 0.32\text{ m}^{-1}$, $S = 0.017\text{ nm}^{-1}$), and non-algal particles (NAP, $a(400\text{ nm}) = 0.09\text{ m}^{-1}$, $S = 0.011\text{ nm}^{-1}$). Based on data and models from [14, 196–198].

absorption at a reference wavelength λ_0 and S is the spectral slope, typically 0.006–0.013 nm^{-1} for NAP and 0.012–0.022 nm^{-1} for CDOM, depending on the composition [14, 198]. For CDOM, the exponentially-shaped spectrum is thought to arise from a superposition of different bonds within the long organic molecules. Short bonds absorb at shorter wavelengths, while resonances of multiple bonds absorb at longer wavelengths. Short bonds are more common and thus the absorption decreases with λ [14].

$$a(\lambda) = a(\lambda_0)\, e^{-S(\lambda-\lambda_0)} \tag{1.8}$$

Elastic scattering by particles is relatively spectrally flat, but highly directional [201]. The scattering coefficient decreases slightly with wavelength, with a spectral slope related to the average particle size [32, 202]. Rayleigh scattering by water molecules scales with λ^{-4} and is only significant at blue and UV wavelengths, since $b_{\text{water}}(\lambda > 350\text{ nm}) < 0.02\text{ m}^{-1}$ [203]. The *volume scattering function* $\beta(\hat{\xi})$ (VSF, in $\text{m}^{-1}\text{ sr}^{-1}$) describes the distribution of light across different scattering angles. $\beta(\hat{\xi})$ is the product of b (magnitude, as before) and the phase function $\tilde{\beta}(\hat{\xi})$: $\beta(\hat{\xi}) = b\tilde{\beta}(\hat{\xi})$.

For unpolarised light, scattering in water is typically azimuthally symmetric and β varies only with the scattering angle ψ [14], as in Figure 1.7. The angular dependence of β is dictated by the morphology and internal structure of particles, and measuring at multiple angles probes these properties [164, 204]. In remote sensing, only light scattered back out of the water is observed, which is described by the *backscattering coefficient* b_b. Mathematically, b_b is the integral of $\beta(\psi)$ over the angles $90° \leq \psi \leq 180°$. Natural waters tend to be highly forward-scattering, with relative backscattering coefficients $\frac{b_b}{b} \approx 0.01$ [204, 205]. Elastic scattering induces linear polarisation, particularly at $\psi \approx 90°$ where $M_{I\to Q} \geq 0.5$ for pure sea water and many types of sediment and phytoplankton [164, 167].

Unlike elastic scattering, inelastic processes like fluorescence and Raman scattering do not conserve wavelength. A photon of wavelength λ is absorbed and another is re-emitted with a wavelength λ'. In the visible range, ~2% of the solar irradiance is re-emitted through

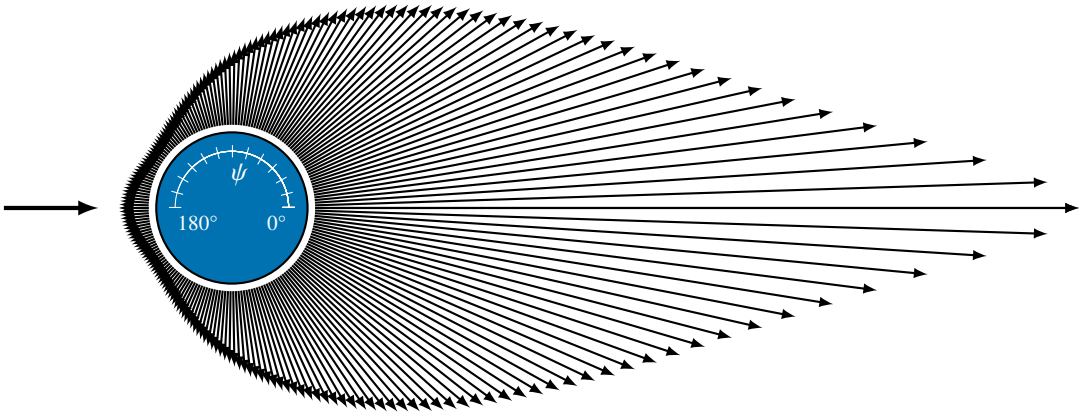

Figure 1.7: Scattering of light in water. Light coming in from the left gets scattered in all directions. The scattered arrow length scales logarithmically with the phase function $\tilde{\beta}(\psi)$ at scattering angles ψ. A parameterised version of the empirical Petzold turbid phase function from San Diego harbour was used [204, 205], which is azimuthally symmetric. The three-dimensional phase function can be visualised by rotating this image about the horizontal axis.

fluorescence, primarily by CDOM and phytoplankton pigments [165]. Phytoplankton species can be distinguished by their distinctive re-emission spectra, for example using the ratio between re-emission at 660 nm vs. at 684 nm when illuminated with 445 nm light [53]. Fluorescence is one of the most common techniques for in-situ measurement of chl-a (Section 1.1.2). Raman scattering by water contributes up to several percent of the total light field, varying with wavelength [96]. Fluorescence and Raman scattering are depolarising, which is used to distinguish light emitted through these processes from elastic scattering [165].

Constituent concentrations and properties can be derived from IOP measurements. For example, measurements of the a(676 nm) peak height (Figure 1.6) can be inverted to obtain phytoplankton concentrations [52]. Flow-through instruments like the LISST and AC-s provide high-quality in-situ IOP data for these purposes [28, 40]. However, sampling is often laborious and expensive (Section 1.1.4). Remote sensors can complement IOP measurements by measuring the *apparent optical properties* (AOPs) of water, the results of the interaction between incoming light and the IOPs [14]. As described below, AOP measurements can be used to estimate the IOPs and constituent concentrations.

1.3.2 Reflectance

The most important apparent optical property in remote sensing is *reflectance*, the ratio of water-leaving over downwelling (ir)radiance. Light impinging on water is directly reflected off the surface or penetrates into the water column. The latter component is then scattered and absorbed by the water and its constituents. A fraction of this light is scattered back out of the water, either directly by a single backscattering event or indirectly through multiple scattering events. This component is called the *water-leaving radiance* L_w and holds information on the IOPs. Directly reflected light (*glint*) does not hold information on the IOPs and is not part of L_w, but acts as a source of uncertainty. The relative contribution of glint to the total upwelling radiance, which includes glint and L_w, ranges from near-zero to near-100% depending on viewing conditions, IOPs, and wavelength [206]. The main challenge in remote sensing of

water is to accurately measure L_w, and from it determine the reflectance [120].

Modern remote sensing of water uses the *remote sensing reflectance* R_{rs}, which is the ratio of L_w over the downwelling irradiance E_d, as in Equation (1.9). R_{rs} is most commonly defined to be in air, just above the water surface, and has units of sr^{-1}. Alternative combinations of (ir)radiances exist but are less popular (Section 5.2). L_w is a directional quantity $L_w(\lambda, \hat{\xi})$, and thus so is R_{rs}. However, R_{rs} is usually only evaluated in a single viewing direction with a narrow field of view (1°–7° diameter), so this directionality is left out [14]. Spectropolarimetric versions of R_{rs} include the reflectance Mueller matrix and the ratio of polarised L_w (defined as $\sqrt{Q^2 + U^2}$) over unpolarised E_d [165].

$$R_{rs}(\lambda) = \frac{L_w(\lambda)}{E_d(\lambda)} \tag{1.9}$$

Strictly speaking, R_{rs} has two wavelength dependencies, namely λ for E_d and λ' for L_w, because of inelastic scattering. For example, fluorescence can shift energy from $E_d(445\,\mathrm{nm})$ to $L_w(685\,\mathrm{nm})$. However, because field measurements are performed using natural broad-spectrum E_d from the Sun and sky, it is not possible to actually determine R_{rs} as a two-dimensional quantity, and the one-dimensional approximation in Equation (1.9) must be used. In edge cases where fluorescence or Raman scattering is the dominant process at a particular wavelength, this approximation can make the interpretation of results less intuitive.

Satellite instruments determine R_{rs} from the top-of-atmosphere (TOA) E_d and L_w. The TOA E_d is well-known from measurements of the extraterrestrial solar irradiance, which is essentially constant over time. The TOA E_d at a given time depends primarily on the current Sun-Earth distance, which is easily calculated from orbital models [97]. The TOA total upwelling radiance is measured at a chosen angle. An atmospheric correction algorithm is used to determine the corresponding surface-level E_d and L_w. Scattering in the atmosphere provides the bulk of the TOA upwelling radiance, with L_w accounting for ≤20% at blue wavelengths. While the contribution of scattering by air is relatively constant over time, absorption and scattering by aerosols is highly variable. Aerosols come in many flavours, including dust, pollen, sea salt, and soot, and accordingly have a wide variety of optical properties. Atmospheric correction algorithms remove the contributions of air, aerosols, and trace gases like ozone to the TOA radiance based on empirical concentrations and optical properties and on models of radiative transfer and aerosol transport through the atmosphere [207]. Atmospheric correction is a high-dimensional problem and thus includes many uncertainties, which are propagated into L_w five- to tenfold and are the primary contributor to uncertainty in satellite-based R_{rs} measurements [186, 208]. In inland and coastal waters, additional uncertainty is introduced by the adjacency effect, where radiance from targets outside the field of view (FOV) of a pixel, such as clouds or land, is scattered into the FOV by the atmosphere [188]. Currently, the typical uncertainty on satellite measurements of R_{rs} is ~5% at blue and green wavelengths, although the reproducibility between different instruments is worse [88].

Terrestrial and airborne instruments determine R_{rs} from (near-)simultaneous measurements of L_w and E_d. The technique most relevant to this thesis is terrestrial above-water radiometry (Figure 1.8), in which measurements of the total upwelling radiance L_u and sky radiance L_{sky} are used to determine L_w [209], as in Equation (1.10). For a full review of terrestrial techniques, the reader is referred to [97, 120].

$$R_{rs}(\lambda) = \frac{L_u(\lambda) - \rho L_{sky}(\lambda)}{E_d(\lambda)} \tag{1.10}$$

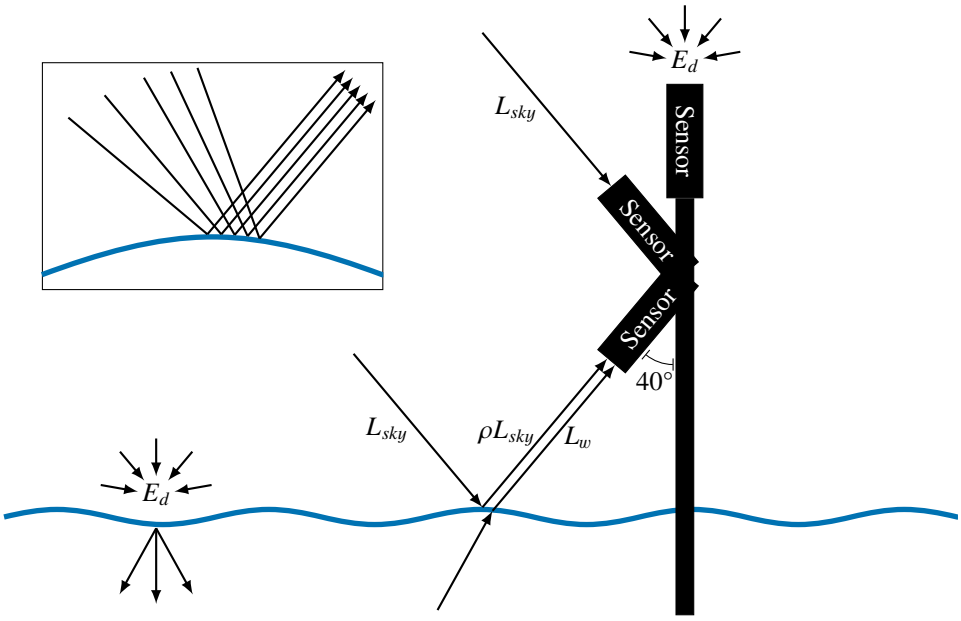

Figure 1.8: Schematic representation of an above-water radiometry setup. Downwelling irradiance E_d impinges on the water surface and propagates into the water column (bottom left), while simultaneously being measured by an E_d sensor (top right). A sensor looking downwards measures the upwelling radiance L_u, which is the sum of the water-leaving radiance L_w and the directly reflected sky radiance ρL_{sky}, with ρ the surface reflectivity. A third sensor, looking upwards, measures L_{sky} directly. As shown in the inset, the reflected sky radiance ρL_{sky} originates from different locations on the sky due to specular reflectance from different wave facets.

The surface reflectivity ρ expresses the proportion of L_{sky} that is directly reflected into the sensor field of view, typically 0.025–0.030 but highly dependent on viewing conditions [209, 210]. For pure, still water, L_{sky} is directly reflected from only a single direction and the Fresnel reflectance can be used. However, real water surfaces have waves. As illustrated in the inset of Figure 1.8, each facet of a wave corresponds to a different reflection angle, and wavy surfaces thus reflect light from a wide area on the sky, depending on the exact viewing geometry and wave conditions. The variability of ρ with wave conditions, specifically wind speed, is minimised by observing at $\theta = 40°$ from nadir or zenith (in elevation) and $\phi = 135°$ in either direction from the Sun (in azimuth) [209, 211].

Distinguishing between water-leaving and directly reflected radiance remains a major challenge [120, 209]. The accuracy of above-water measurements is improved by empirically determining ρ for each measurement and by subtracting an additional offset Δ from the right-hand side of Equation (1.10). Δ and ρ can be determined from imaging of wave conditions and from spectral analysis of L_u at wavelengths with known atmospheric features. Using these methods, the typical error on R_{rs} induced by glint can be reduced to 6–8% [210]. Above-water radiometry is discussed in more detail in Chapter 4.

1.3.3 Constituent retrieval and inversion

R_{rs} is proportional to the ratio of b_b over a, or some empirical function thereof, as shown in Equation (1.11). Traditionally, the former relation is used in phytoplankton-dominated Case I waters, and the latter in Case II waters, but this distinction is controversial [212]. The relation can be understood intuitively – highly absorbing waters (large a) appear dark because few photons make it out, whereas highly scattering waters (large b_b) appear bright because photons are quickly scattered back out. The proportionality constants between R_{rs} and the IOP ratios vary slightly due to environmental conditions, constituent concentrations, and viewing geometry [212]. Sometimes, a polynomial function is used instead of a linear relation. An exact inversion from R_{rs} to a, b_b requires a full radiative transfer simulation accounting for all radiative processes including detailed knowledge of the IOPs and their dependence on viewing angle and depth, but the relations shown in Equation (1.11) provide an adequate approximation [14, 96]. It is important to note that passive remote sensing is only sensitive to the top layer of the water column, since few photons penetrate deep into the water, and of those that do, even fewer make it back out [213]. The penetration depth ranges from centimetres in highly turbid or absorbing waters to ~50 m in clear ocean waters and is highly wavelength-dependent [96].

$$R_{rs}(\lambda) \propto \frac{b_b(\lambda)}{a(\lambda)} \qquad R_{rs}(\lambda) \propto \frac{b_b(\lambda)}{a(\lambda) + b_b(\lambda)} \tag{1.11}$$

The spectral signatures of different constituents in the IOP spectra propagate into R_{rs} (Figure 1.9), and are exploited to retrieve constituent IOPs and concentrations. Strong absorption from water decreases R_{rs} with wavelength for $\lambda > 600$ nm in clear waters with low chl-a and SPM concentrations. In CDOM-rich waters, R_{rs} at blue wavelengths ($\lambda < 500$ nm) is depressed by CDOM[3] and NAP absorption; S_{CDOM} can be estimated from the spectral slope in R_{rs} at these wavelengths. Phytoplankton lowers R_{rs} at wavelengths where chl-a absorbs strongly (Figure 1.6), particularly around 443 nm and 665–675 nm [213]. Fluorescence can increase R_{rs} in specific bands, such as around 680–690 nm in some of our data from around Lake Balaton (Section 4.2.2). Different pigments have specific absorption and fluorescence bands, which are used to distinguish phytoplankton species and functional groups [42, 49, 214], as discussed below. Particulate backscattering increases R_{rs} across the visible range [96], and b_b, TSM, and related quantities can be estimated from R_{rs} at red wavelengths where particles are the dominant scatterers [32, 213]. More detailed information can be obtained if spectral features specific to a constituent are known [215] or with prior information on the target, for example on the typical local phytoplankton community composition [216].

A wide range of retrieval algorithms are used in practice, ranging from empirical to analytical [13, 14, 88, 195, 213, 218, 219]. Empirical algorithms are derived by comparing remote observations with field measurements or simulations (Section 1.3.4), without additional inputs. This makes them relatively quick and simple to derive, but less portable as they depend, explicitly or implicitly, on assumptions that only hold locally or under specific conditions. Many empirical algorithms are *band-ratio algorithms*, relating a single parameter to the ratio of R_{rs} at two or more wavelengths [220–223]. A major advantage of band-ratio algorithms is their robustness to correlated uncertainties and biases in L and R_{rs}, which may divide out

[3] Hence the old name *gelbstoff* or *yellow substance*.

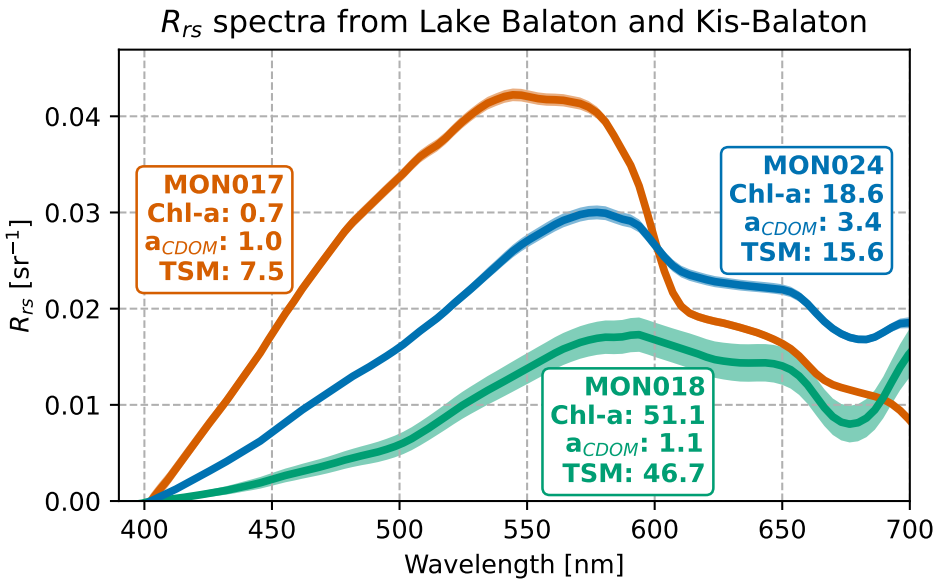

Figure 1.9: R_{rs} spectra from Lake Balaton (MON017, MON024) and Kis-Balaton (MON018) taken with TriOS RAMSES spectroradiometers during the 2019 MONOCLE field campaign [217]. Each line represents the median spectrum from a given station, the shaded areas represent the standard deviations. Biogeochemical data (chl-a concentration in mg m^{-3}, a_{CDOM}(440 nm) in m^{-1}, and TSM in g m^{-3}) from in-situ samples are also provided. As discussed in Section 1.3.3, CDOM and phytoplankton absorption induce a slope in R_{rs} at $\lambda \leq 500$ nm, with R_{rs} lower at the stations richer in CDOM and chl-a. Inflection points in the water absorption spectrum around 600 and 650 nm (Figure 1.6) are seen in R_{rs}, as is the chl-a absorption peak at 665 nm. Furthermore, MON024 is brighter than MON017 at $\lambda > 600$ nm due to increased particulate scattering. TSM at MON018 is 3× that at MON024 but R_{rs} is lower, because of differences in the suspended matter composition – Kis-Balaton contains mostly algal particles while western Lake Balaton contains many bright chalk particles [27]. Further examples of R_{rs} spectra are shown in Figures 4.2 and 5.2.

(Chapter 4). Conversely, analytical algorithms are grounded in radiative transfer models and are thus based on physics, theoretically making them more portable to different applications but also vulnerable to uncertainty in prior information. Any uncertainty in the IOPs used to derive the analytical model will propagate into every retrieved value. Semi-analytical models combine the two approaches by supplementing observations with prior information such as typical IOPs at a certain site [27, 224–226]. Generally, empirical algorithms retrieve one or more constituent concentrations, while (semi-)analytical algorithms focus on retrieving IOPs [213]. This thesis is focused primarily on empirical band-ratio algorithms, which are the most appropriate and popular type for multispectral data from consumer cameras (Chapter 4) and the type most commonly applied through spectral convolution (Chapter 5).

Most band-ratio algorithms for chl-a make use of the absorption peaks around 443 nm and 665 nm, the fluorescence peak around 680 nm, and wavelengths with minimal absorption by phytoplankton, CDOM, and particulate matter such as 550 nm and 700 nm [213,220]. For example, the OCx algorithms relate chl-a to a function of the ratio between blue- and green-band R_{rs} from any ocean colour sensor [220]. Increased chl-a leads to an increase in a(443 nm) and

thus a decrease in $R_{rs}(443\,\text{nm})$, while $R_{rs}(550\,\text{nm})$ remains relatively unchanged, leading to a decrease in the $\frac{R_{rs}(443\,\text{nm})}{R_{rs}(550\,\text{nm})}$ ratio. In Case I waters, where chl-a and CDOM covary and thus the overlap between their absorption spectra is not an issue [213], OCx algorithms can predict chl-a to within a factor of ~1.74 compared to in-situ samples [220]. In lakes with little chl-a (0–10 mg m^{-3}) and high CDOM and NAP absorption, meaning the Case I assumption does not hold, the OCx chl-a estimate is inaccurate [218]. Many alternative chl-a algorithms exist for specific sites. For example, an exponential function of the Sentinel-2/MSI red-green band ratio (B3/B4) predicts chl-a with an accuracy compared to in-situ data of 20% in Lake Ba Be in Vietnam [221]. The target accuracy for chl-a retrieval compared to in-situ measurements was 35% for SeaWiFS and 10–30% (Case I) or 10–70% (Case II) for Sentinel-3/OLCI. Most applications require an uncertainty in chl-a of 10–25% [88].

Empirical retrieval algorithms also exist for many other parameters. For example, the concentration of the cyanobacterial pigment phycocyanin can be determined from the 709/620 nm reflectance band ratio with an accuracy of 20% (typical difference) compared to in-situ samples, although the accuracy is worse when other phytoplankton species and pigments are more abundant [214]. Algorithms for particulate b_b and TSM often use the absolute R_{rs} in one or multiple red–NIR bands, where TSM is the dominant optical component [213], or a red-blue band ratio [34]. In one study in the North Sea, R_{rs} at any wavelength from 670–750 nm predicted TSM to within 30% accuracy compared to in-situ data [227]. Lastly, a_{CDOM} and S_{CDOM} at various UV–blue wavelengths can be determined from the 412 nm-670 nm and 412 nm-547 nm R_{rs} band ratios to within 24–30% (a) and 8–10% (S) accuracy [222]. As with chl-a, there are many different retrieval algorithms for the aforementioned constituents, derived for various sites and instruments. Simultaneous retrieval of multiple parameters is achieved by taking advantage of the linear summability of IOPs and the existence of wavelengths with minimal overlap between IOP spectra [228]. Finally, some algorithms convert the R_{rs} spectrum into a lower-dimensional colour measure before retrieval, such as central wavelength, hue angle, or blueness [10, 229, 230]. For a review of empirical and semi-analytical retrieval algorithms for chl-a and other algal pigments, TSM, and CDOM, the reader is referred to [213, 231].

In general, empirical algorithms reduce the vast biogeochemical parameter space, which includes concentrations of many different phytoplankton species, dissolved organic and inorganic matter, and various types of particles, into a handful of spectral bands. This simplification is possible in practice due to covariance between parameters and constraints on the parameter space in specific sites. However, this fundamentally means that empirical algorithms perform well only in the conditions they were designed and validated for, and poorly when the underlying assumptions do not hold. Analytical and semi-analytical approaches that include prior information provide a more robust alternative, although these too are limited by the accuracy of said prior information. Additionally, measuring hyperspectrally and with a wider wavelength range, for example in the UV range for CDOM, provides a wider input space, although only if measurement uncertainties are sufficiently small [87, 144, 232]. Machine learning techniques, including neural networks, are increasingly popular for deriving new algorithms and combining existing ones [219, 233]. Particularly important for future algorithm development is the generation of in-situ validation data sets with greater size and diversity [218]. For a general review of retrieval and inversion algorithms based on spectral features in R_{rs}, the reader is referred to [41, 131, 213, 231, 234].

Currently, polarisation is largely neglected in remote sensing of water, although many proof-of-concept studies have shown that including polarisation improves the accuracy of

measurements of organic and inorganic particle shape, size, and composition [163, 174, 182, 235, 236]. The use of multiangular spectropolarimetry for retrieval of particle properties is more common in the atmospheric aerosol research community, where spaceborne, airborne, and ground-based spectropolarimeters provide data products including aerosol optical depth, effective particle radius, complex refractive index[4], and aerosol layer height, separated between fine- and coarse-mode particles [125, 132, 237]. In water research, spectropolarimetry is seen as a high-potential technique for the near future [165, 238], particularly the upcoming PACE mission with its SPEXone and HARP-2 instruments [86]. As discussed in Section 1.2.3, SPEXone and HARP-2 are primarily designed for aerosol science, which will improve the retrieval of water reflectance and constituents by reducing the uncertainty due to atmospheric correction [185, 188]. However, these two instruments, especially when used in conjunction with OCI, will also enable new water research through joint atmosphere-water retrieval algorithms [186, 187, 239]. For example, coccolithophores polarise scattered light depending on their degree of calcification, which is under pressure from ocean acidification [21]; thus, polarimetric remote sensing could be used to assess coccolithophore health and the ecological impact of acidification globally [20]. At a 50°–60° viewing angle, P_L is correlated with the $\frac{c}{a}$ IOP ratio and polarisation can thus be used to distinguish between absorption and scattering [174]. Lastly, polarisation can be used to characterise and minimise the error induced by glint, since direct reflections are highly polarised compared to water-leaving radiance, although as in Figure 1.8, this is complicated by wave motion [174, 211, 240].

1.3.4 Validation

A vital aspect of remote sensing is *validation*, assessing the performance of an instrument or algorithm under realistic conditions. Data and retrieved parameters are compared with those from a different instrument or algorithm, or with in-situ sampling or simulated data. When different methods or instruments agree to within measurement uncertainties, closure is achieved [40, 88].

Validation data are obtained during dedicated campaigns, from large instrument networks, or from aggregated archival data. For example, Chapter 4 describes a three-day campaign on and around Lake Balaton, Hungary, during which we validated L, R_{rs}, and colour measurements from smartphone cameras. Instrument networks like AERONET-OC and Argo provide regular, consistent optical and biogeochemical validation data from many diverse sites [80, 117]. Lastly, archives such as LIMNADES, PANGAEA, SeaBASS [241], and Zenodo contain diverse data sets from many different cruises and instruments, which are sometimes bundled together into larger data releases [50]. These archival data can be used again for novel research, such as in Chapter 5, which discusses instrument validation through intercomparisons between multi- and hyperspectral data.

The research described in this thesis was performed within the Horizon 2020 project MONOCLE[5], which had as one of its aims to improve the validation of remote sensing data. To this end, several low-cost in-water [242] and above-water spectroradiometers, including iSPEX 2 (Chapter 6), were developed and tested in the field (Figure 1.10). The low cost of these instruments makes them attractive for autonomous use, such as mounting one on a

[4] The complex refractive index consists of a real part (Section 1.2.2) and an imaginary part describing absorption.

[5] Multiscale Observation Networks for Optical monitoring of Coastal waters, Lakes and Estuaries, https://monocle-h2020.eu/

ferry, for large-scale deployment, and for use by citizen scientists. This in turn increases the scale and diversity of the obtained validation data, while also providing the community with new instruments for novel research.

1.4 Citizen science

Citizen science or *participatory research* is the involvement of non-professionals (citizens) in the scientific process. There are several types of involvement, ranging from crowdsourcing, where citizens collect data for professional researchers, to co-creation, where the citizens are involved in various aspects of formulating and investigating a research question [95, 243]. Citizen science projects exist across this spectrum in many scientific fields, particularly in biological, ecological, and geographical research [244]. On a metalevel, research into citizen science itself is focused on determining and optimising participant motivation and retention; data quality, quantity, and value; and the interaction between professional and citizen scientists [95, 245–247].

Citizen involvement in science brings many benefits both to the citizens and to professional scientists, and provides insights that could not be obtained by either group alone. Crowdsourcing greatly expands the amount and diversity of data that can be gathered, which is desirable in most fields of environmental science (Sections 1.1.4 and 1.3.4). For example, in the first measurement campaign using the iSPEX smartphone spectropolarimeter, on 8 July 2013, 6 007 measurements of aerosol optical depth throughout the Netherlands were conducted by citizen scientists [94]. To obtain similar levels of spatial coverage with professional ground-based sensors would be prohibitively expensive, while satellites could not provide the spatial resolution and revisit time. Involvement of citizens in the processing, analysis, and interpretation of data provides professional scientists with novel insights [248, 249], such as local information about a measurement site that an external researcher otherwise would not have known (Section 1.3.3). Simultaneously, the citizen participants gain a greater understanding of the scientific process in general and their project in particular, which in turn empowers them as social and political stakeholders [66, 250, 251], as encouraged in the United Nations Sustainable Development Goals and European Green Deal [252, 253]. It is important to ensure that all parties, citizen and professional alike, fulfil their motives, and to prevent negative impacts such as interpersonal conflicts from occurring [247].

Because of its great importance to society (Section 1.1), water research has always been a popular field for citizen science. Many of these projects are conservation efforts, for example monitoring plastic pollution [77, 254]. Participants' intimate knowledge of their local study site enables them to identify changes, abnormal events, and long-term trends that outside researchers cannot [248, 249]. A major motivation for many participants is a desire to protect their local environment and community, in addition to a desire to learn more and contribute to scientific advances [255, 256]. After all, citizens are the most important societal stakeholders in and funders of water research and policy [1]. Citizen science benefits from having many, diverse participants, but recruiting and retaining them is difficult and demographics are often skewed [257]. For a broader overview of citizen science in water research, the reader is referred to [243, 248, 249, 258]; citizen motivation and retention is discussed further in Chapter 2.

Citizen science benefits from access to low-cost equipment, with the Secchi disk for water transparency measurements and Forel-Ule scale for water colour as prominent examples.

Figure 1.10: The MONOCLE team performing validation measurements at Loch Leven, United Kingdom, in August 2018. Three boats with various hand-held and mounted spectroradiometers as well as in-situ bio-optics instruments are on the lake, with three UAVs carrying hyper- and multispectral cameras in the sky above. The measurements were performed during a Sentinel-2 satellite overpass. Photograph courtesy of Stefan Simis.

The Secchi disk was first used by papal astronomer Angelo Secchi[6] in 1865 to measure water transparency [259, 260]. It is a white or black-and-white disk, normally ~30 cm in diameter, which is lowered into the water on a rope until it disappears from view. The depth at which it is no longer visible is the *Secchi disk depth* z_{SD}. The value of z_{SD} is related to the beam attenuation coefficient c (Section 1.3.1) and the diffuse attenuation coefficient K_d, an AOP describing the change in E_d with depth, although the exact relation remains a matter of debate [14, 259, 261–263]. z_{SD} is deepest (>80 m) in clear ocean waters and shallowest in turbid Case II waters with heavy particle loads [261]. For example, z_{SD} in highly turbid Lake Balaton (Chapter 4) can be as shallow as 20 cm [264]. The simplicity of the Secchi disk makes it ideal for citizen science since participants can 3D-print or craft their own disk [265, 266]. Variants such as the Secchi tube are also in use [66]. A new smartphone application for Secchi disk measurements[7] was developed within the aforementioned Horizon 2020-funded MONOCLE project.

The Forel-Ule (FU) scale is a standardised 21-colour scale to classify water colour, first devised in the 1890s by François Forel and Willi Ule [267, 268] and to some extent revived in the 2010s by Marcel Wernand [269]. Measurements are performed by comparing the apparent colour of the Secchi disk at $\frac{z_{SD}}{2}$ with a physical colour scale. The FU scale can be used without a Secchi disk by looking straight down the water column, provided the bottom is not visible, but this biases the result by up to 2 FU [270]. Century-long FU time series with global coverage enable the study of long-term changes in ocean colour and chl-a concentration [10, 271]. The FU scale is also used for validation of remote sensing products [270, 272] since multi- or hyperspectral R_{rs} can be converted to FU through spectral convolution (Chapter 5). Use of the FU scale in citizen science is discussed further in Chapters 2 and 4.

Smartphone cameras are particularly promising as low-cost spectroradiometers. Recent years have seen a flurry of smartphone-based research in environmental science [273] and many other fields (Section 3.1). Both professional and citizen science benefit from the high-end cameras in modern smartphones. As discussed in Sections 1.2 and 3.2, smartphone and other consumer cameras typically have three spectral bands, red-green-blue or RGB, covering the visible range. These capabilities can be expanded with spectroscopic add-ons [98, 143]. For example, the iSPEX add-on enabled spectropolarimetry on smartphones and, as mentioned above, was used to crowdsource AOD [94]. Citizen scientists participated out of an interest in the science and a desire to contribute to the field [256]. Unfortunately, the quality of individual observations was limited by software restrictions on the smartphone cameras, although the uncertainty was reduced by averaging over multiple devices. Furthermore, the add-on did not fit on newer smartphones. In water research, the HydroColor and EyeOnWater apps have been used by thousands of professional and citizen scientists to measure R_{rs} and water colour [121, 274]. Validation studies of both have shown agreement with reference instruments, but have also found large inaccuracies and uncertainties upwards of 30% [275, 276]. In all three examples, issues of data quality stem from the need to use JPEG data, which are heavily compressed and non-linear. These limitations are addressed in this thesis in Chapters 3, 4, and 6.

Achieving a high impact with citizen science requires trust in the robustness of methods, data, and results [277]. Trust can be achieved through standardisation of the data acquisition and processing, for example by providing participants with standardised equipment [77].

[6] Better known among astronomers for his contributions to spectroscopy and solar physics and his catalogue of double stars [259].

[7] https://monocle-h2020.eu/Sensors_and_services/Mini-secchi_disk

Keeping the methodology similar to that of professional measurements, such as HydroColor following the standard (Mobley) protocol for R_{rs} measurements [121, 209], further increases trust. At the same time, data quality is highest when the methodology is simple [254, 277]. Trust in results requires consistent reporting, using standard quantities [77] and including uncertainties [278], and rigorous validation by participants and third parties [275, 276]. Citizen scientists' trust in results is also influenced by interpersonal factors [279]. Well-designed citizen science projects can achieve a data quality similar to professional science [277]. This thesis discusses standardisation, data quality, and uncertainty in citizen science data in Chapters 2, 3, and 4.

1.5 This thesis: Accessible remote sensing of water

The aim of this thesis is to investigate and improve accessibility and uncertainty in remote sensing and citizen science, so that these techniques can better deliver the desired improvements to cost, scale, and reproducibility of water research (Section 1.1.4). Accessibility is improved by accounting for disability in citizen science (Chapter 2) and by developing consumer cameras as low-cost instruments for remote sensing by professional and citizen scientists (Chapters 3, 4, and 6). Increased accessibility is associated with a lower cost and wider scale of water research. We assess and reduce the uncertainty in measurements by citizen scientists and measurements from consumer cameras (Chapters 2, 3, and 4), as well as the uncertainty in comparing and combining data from different professional instruments (Chapter 5). Better characterised and reduced uncertainty leads to higher reproducibility. Chapter 7 provides a general synthesis, discussion, and future outlook. Short summaries of each chapter are provided below.

The research described in this thesis was performed over a 4-year period, from 2018 to 2022, within the MONOCLE project. Due to various internal and external factors, most prominently the COVID-19 pandemic, our original plans had to be adapted multiple times and we were unable to perform much of the planned field work and citizen science experiments. As a result, the research topics of Chapters 2–6 are quite diverse. However, as described above, they all deal with different aspects of two core topics, namely accessibility and uncertainty in remote sensing of water. The chapters are arranged by the dimensionality of their respective data, from multispectral (Chapters 2–4) through hyperspectral (Chapter 5) to spectropolarimetric (Chapter 6), but can be read in any order.

Chapter 2. Citizen science with colour blindness: A case study on the Forel-Ule scale. Colour vision is often used in citizen science, including Forel-Ule measurements (Section 1.4). However, up to 1 in 11 participants have deficient colour vision (Section 1.2.2). In this chapter, we simulate the effects of colour blindness on Forel-Ule measurements to quantify the resulting uncertainty. Based on the results, we suggest likely effects on participant motivation and retention, and offer general recommendations on improving accessibility and quantifying uncertainty in citizen science [280].

Chapter 3. Standardised spectral and radiometric calibration of consumer cameras. Consumer cameras, particularly onboard smartphones and UAVs, are now commonly used as scientific instruments (Section 1.4). However, their data processing pipelines are not optimised for quantitative radiometry and their calibration is more complex than that of scientific

cameras (Section 1.2). The lack of a standardised calibration methodology limits the interoperability between devices and, in the ever-changing market, ultimately the lifespan of projects using them. In this chapter, we present a standardised methodology and database (SPECTACLE) for spectral and radiometric calibrations of consumer cameras. The methodology is applied to seven popular cameras to characterise their performance and quantify uncertainties. Through calibration and the use of RAW data, we lay the groundwork for using consumer cameras to perform professional-grade spectroradiometry [281].

Chapter 4. Accuracy and reproducibility of above-water radiometry with calibrated smartphone cameras using RAW data.
In this chapter, we apply the results and recommendations from Chapter 3 to above-water radiometry. We measure R_{rs} and water colour on and around Lake Balaton, Hungary, with two smartphones and two hyperspectral reference instruments for validation (Section 1.3). We quantify the uncertainty, reproducibility, and accuracy of the resulting data and compare these to professional spectroradiometers and existing citizen science approaches (Sections 1.2 and 1.4). We find that smartphone cameras perform similarly to professional instruments. The typical uncertainty of individual smartphone measurements is ≤5% in radiance, 1.9–8.1% in R_{rs}, and 0.5–1.9% in R_{rs} band ratios. The typical difference between two smartphones is 6.9% in radiance, 5.5% in R_{rs}, and 2.9% in R_{rs} band ratios. Lastly, the typical difference between smartphone and reference data is ≤19% in radiance, ≤13% in R_{rs}, and ≤1.9% in R_{rs} band ratios, barring one outlier. Based on these results, we offer practical recommendations for using consumer cameras in professional and citizen science [282].

Chapter 5. Biases from incorrect reflectance convolution.
Reflectance measurements from hyperspectral instruments are converted to multispectral bands (Section 1.2.2) through spectral convolution. This is done to combine time series, validate instruments, and apply retrieval algorithms (Section 1.3). However, convolution is often done incorrectly, with reflectance itself convolved rather than the underlying (ir)radiances. In this chapter, the resulting error is quantified for simulated and real instruments. Significant biases, up to 5%, are found. Based on these results, we suggest that this error was partially responsible for uncertainties found in previous work and recommend that future work apply spectral convolution correctly [283].

Chapter 6. A universal smartphone add-on for portable spectroscopy and polarimetry: iSPEX 2.
In this chapter, we present a new smartphone spectropolarimeter, iSPEX 2. It succeeds the original iSPEX add-on (Section 1.4). The optical design is presented and the manufacturing process is detailed. Through universal smartphone support and a data processing pipeline based on Chapter 3, we aim to improve the accessibility and data quality compared to the original. An initial validation measurement is presented as a proof of concept. Finally, we suggest possible applications of iSPEX 2 for professional and citizen science [284].

Chapter 7. General discussion and future outlook.
In this chapter, we synthesise the overall findings of Chapters 2–6 and discuss them relative to the current state and future direction of the field. Initial findings from a follow-up project on spectropolarimetry of floating debris are also presented. Finally, the major conclusions and recommendations of this thesis are summarised.